JGR Earth Surface

RESEARCH ARTICLE
10.1029/2021JF006466

Wave Dissipation and Mean Circulation on a Shore Platform Under Storm Wave Conditions

Laura Lavaud[1], Xavier Bertin[1], Kévin Martins[2], Marc Pezerat[1], Thibault Coulombier[1], and Denis Dausse[1]

[1]UMR 7266 LIENSs, CNRS/La Rochelle Université, La Rochelle, France, [2]UMR 5805 EPOC, CNRS/Université de Bordeaux, Pessac, France

Key Points:

- A new field data set collected during storm wave conditions on a shore platform instrumented from 10 m water depth up to the shoreline
- Wave bottom friction explains about 40% of the total wave energy dissipation across the shore platform and reduces the wave setup
- The contribution of the wave-induced circulation to the wave setup is enhanced on the rough bottom and increases with the bed slope

Correspondence to:
L. Lavaud,
laura.lavaud@univ-lr.fr

Citation:
Lavaud, L., Bertin, X., Martins, K., Pezerat, M., Coulombier, T., & Dausse, D. (2022). Wave dissipation and mean circulation on a shore platform under storm wave conditions. *Journal of Geophysical Research: Earth Surface*, *127*, e2021JF006466. https://doi.org/10.1029/2021JF006466

Received 6 OCT 2021
Accepted 17 FEB 2022

Author Contributions:

Conceptualization: Laura Lavaud, Xavier Bertin, Kévin Martins
Formal analysis: Laura Lavaud
Investigation: Laura Lavaud, Xavier Bertin, Kévin Martins, Marc Pezerat, Thibault Coulombier, Denis Dausse
Methodology: Laura Lavaud, Xavier Bertin, Kévin Martins
Software: Laura Lavaud, Kévin Martins, Marc Pezerat
Supervision: Xavier Bertin, Kévin Martins
Writing – original draft: Laura Lavaud
Writing – review & editing: Xavier Bertin, Kévin Martins, Marc Pezerat

Abstract While wave processes on shore platforms have been recently advanced by a number of field-based studies, few attention has been paid to the role of bed roughness on wave dissipation and wave setup dynamics in these environments. This study reports on a new field experiment conducted under storm wave conditions on a gently sloping shore platform which was instrumented from 10 m water depth up to the shoreline. Data analyses are complemented with numerical simulations performed with a 3D fully coupled modeling system using a vortex force formalism to represent the effects of short waves on the mean circulation. An accurate representation of wave dissipation by both depth-induced breaking and bottom friction is found essential to reproduce the transformation of short waves across the platform and the resulting wave setup. Wave energy dissipation by bottom friction is dominant in the subtidal part of the platform and contributes to about 40% of the total wave energy dissipation. The enhanced wave bottom friction on the platform decreases the wave height before breaking, which reduces the contribution of wave forces to the wave setup compared to a smooth bottom (mechanism 1). Conversely, an idealized analysis of the cross-shore momentum balance reveals that the wave-induced circulation increases the wave setup, this process being enhanced on a rough bottom (mechanism 2). The contribution of mechanism 2 increases with the bottom slope, accounting for up to 26% of the wave setup for a 1:20 sloping shore platform, and overcoming mechanism 1.

Plain Language Summary In the nearshore, the dissipation of short waves controls the mean circulation by generating currents but also a rise of the mean water level along the shoreline, a process known as the wave setup. Waves and wave-induced processes on shore platforms can be different from that on sandy beaches, principally due to a higher bed roughness. This study reports on a new field experiment conducted under storm wave conditions (short waves reaching 6 m at 50 m depth) on a gently sloping shore platform which was instrumented from 10 m water depth up to the shoreline. Data analyses are complemented with numerical simulations performed with a three-dimensional modeling system coupling a wave and circulation models. The results show that wave bottom friction occurring on the platform explains 40% of the total wave energy dissipation, which reduces the contribution of wave dissipation to the wave setup (mechanism 1). Conversely, further analysis reveals that depth-varying currents forced by waves increase the wave setup, the rough bottom making this mechanism stronger (mechanism 2). Mechanism 2 counteracts mechanism 1 and becomes even dominant as the bottom slope increases, accounting for up to 26% of the wave setup for a 1:20 sloping shore platform.

1. Introduction

Shore platforms are distinctive landforms of rocky coast environments. These erosional rock surfaces are found within or close to the intertidal zone and are usually backed by cliffs, but can also be backed by beaches, dunes or coastal structures. They are generally classified into two different types: gently sloping platforms that extend in the subtidal zone without a break in slope (Type A), and sub-horizontal platforms with a sharp seaward edge (Type B) (Sunamura, 1992). Sloping platforms are predominantly found in meso to macrotidal ranges while sub-horizontal, or Type B, platforms are more common on microtidal coasts (Trenhaile, 1987). While there has been a long-standing debate on which of wave processes or subaerial weathering dominate shore platform development, it is now recognized that these mechanisms act together (Naylor et al., 2010). However, their relative contribution is still unclear, which is partly due to a limited number of field observations of wave processes on shore platforms (Naylor et al., 2010; Stephenson, 2000). Only recently, the understanding of wave processes on shore platforms has advanced thanks to field-based studies examining the transformation of both short (frequencies

> 0.04–0.05 Hz) and infragravity (frequencies < 0.04–0.05 Hz) waves over such environments (Beetham & Kench, 2011; Marshall & Stephenson, 2011; Ogawa et al., 2011, 2015; Poate et al., 2018; Savige et al., 2021; Stephenson & Kirk, 2000; Stephenson et al., 2018; Trenhaile & Kanyaya, 2007). Several of these studies reported the depth-limited character of surf zone waves (Farrell et al., 2009; Ogawa et al., 2011, 2015; Poate et al., 2018) and the strong tidal modulation of wave energy dissipation across platforms (Marshall & Stephenson, 2011; Ogawa et al., 2011). In addition to the effect of tides, the morphological characteristics of the platform, such as the elevation, the gradient, the presence or absence of a seaward edge, and the width (Beetham & Kench, 2011; Marshall & Stephenson, 2011; Ogawa, 2013; Ogawa et al., 2011), have been observed to exert a key control on wave processes, likely explaining the contrasted rates of wave dissipation reported so far in the literature (Ogawa et al., 2012; Stephenson & Kirk, 2000; Stephenson & Thornton, 2005). Poate et al. (2018) combined field data analyses and the application of a 1D model of wave energy flux conservation to investigate bottom roughness effects on wave transformation across several macrotidal platforms of contrasting roughnesses (measured bottom roughness ranging from 0.07 to 0.17 m). The authors suggested that bottom friction is only important outside the surf zone, for very rough, low gradient (<1:50) platforms and weak wave conditions. The latter study, together with the work of McCall et al. (2017), and Gon et al. (2020) on a rocky shore, are some of the very few studies that investigated wave bottom friction on rocky shorelines. In addition, apart from notable exceptions (e.g., Marshall & Stephenson, 2011; Savige et al., 2021), wave transformation has been mainly investigated on the intertidal part of shore platforms, while the rocky substrate can extend further offshore (Kennedy, 2015). Hence, new field deployments combined with numerical simulations are necessary to further understand short-wave dissipation on shore platforms through both wave breaking and bottom friction. This is critical to assess the role of waves in platform erosion and cliff recession, which has been one of the main focus of studies conducted on shore platforms so far (Stephenson & Kirk, 2000; Trenhaile & Kanyaya, 2007), but also to investigate wave-induced hydrodynamics on shore platforms.

In the nearshore, the dissipation of short waves controls the mean circulation by driving longshore currents, undertows as well as rip currents (e.g., see Castelle et al., 2016; Longuet-Higgins, 1970a, 1970b; Svendsen, 1984), and by inducing an increase in mean water levels along the shoreline known as the wave setup (Bowen et al., 1968; Stive & Wind, 1982). The wave setup was first explained physically by the radiation stress formalism of Longuet-Higgins and Stewart (1962, 1964), in which the radiation stress corresponds to the wave momentum flux. On mildly sloping sandy beaches, the wave setup has usually been computed assuming a balance between the cross-shore radiation stress and barotropic pressure gradients in the wave-averaged cross-shore momentum equation (Battjes & Stive, 1985; Lentz & Raubenheimer, 1999). While several studies reported a significant underestimation of the wave setup predicted with this simple approach in very shallow water depths (Guza & Thornton, 1981; Raubenheimer et al., 2001), Apotsos et al. (2007) suggested that wave setup predictions could be improved by including the bottom stress associated with the mean offshore-directed flow (the undertow) in the cross-shore momentum balance. More recently, Guérin et al. (2018) used a 3D phase-averaged modeling system and showed that the wave-induced depth-varying circulation (mostly horizontal advection and vertical mixing) could increase the wave setup when the bottom slope steepens. On shore platforms, wave setup dynamics can be different from that on sandy beaches, principally due to a higher bottom roughness (Buckley et al., 2016; Dean & Bender, 2006). Platform roughness can range from smooth like a sandy beach, to extremely rough similar to coral reefs (Poate et al., 2018). While only one study reported observations of wave setup on shore platforms so far (Ogawa et al., 2015), several roughness effects on waves and wave setup have been identified in coral reef environments which can potentially also operate on relatively rough platforms (e.g., Acevedo-Ramirez et al., 2021; Buckley et al., 2016; Lowe et al., 2005, 2009). In particular, Buckley et al. (2016) conducted high-resolution laboratory measurements of wave setdown and setup across a large bottom roughness fringing reef profile characterized by a 1:5 reef slope. The authors showed that the presence of bottom roughness enhanced wave dissipation by friction which in turn modified radiation stress gradients and resulted in a predicted wave setup 18% lower on average compared to smooth experiments, when the mean bottom stress was neglected in the momentum balance. However, once accounted for, the mean bottom stress, generated by interactions of the undertow with roughness, increased the predicted wave setup by 16% on average. Because of these two opposing mechanisms, the wave setup measured on the reef for both rough and smooth bottoms was similar. These two counteracting effects of bottom roughness on wave setup identified on coral reef environments have yet to be examined on shore platforms. In particular, the wave setup response to, not only the bottom stress, but the overall wave-induced depth-varying circulation should be analyzed in these rough environments.

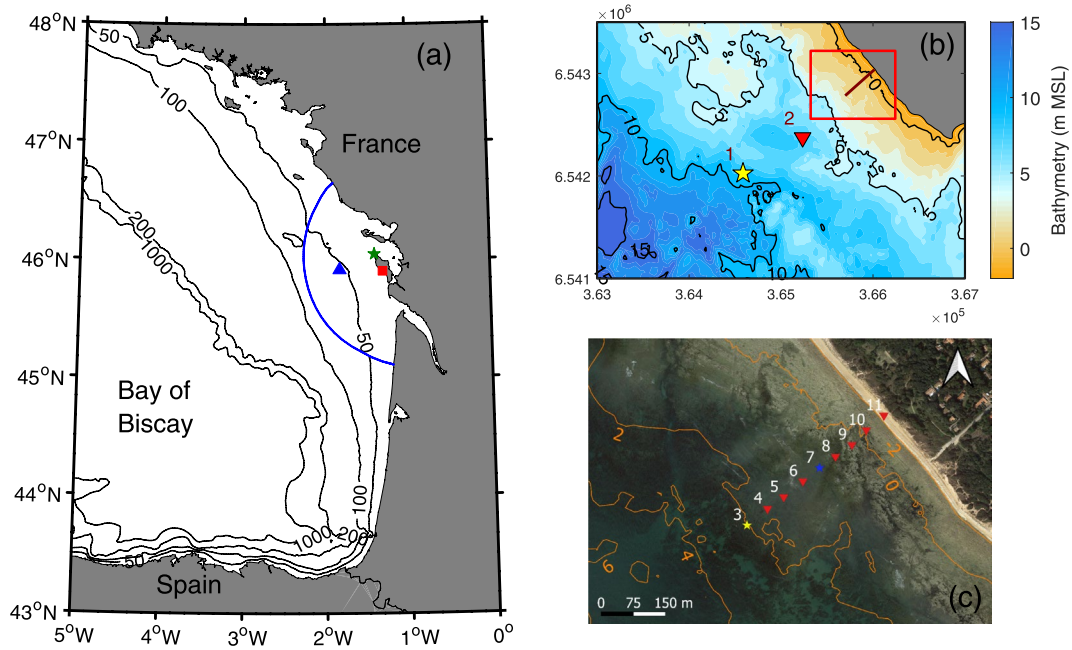

Figure 1. (a) Location of the study area (red square), Oléron wave buoy (blue triangle), meteorological station (green star) and extension of the computational domain (blue line). (b) Bathymetry of the study area relative to mean sea level with location of the subtidal stations (1 and 2), and location of the intertidal zone of the shore platform (red box) with the instrumented transect (brown profile). (c) Zoom on the intertidal zone of the shore platform with location of the intertidal stations along the transect (3–11). The stations shown on panels (b) and (c) were deployed during the field campaign conducted in storm wave conditions.

The aim of this study is to improve the understanding of wave transformation and wave setup dynamics on shore platforms. Through collection of field data, this study contributes to a small number of wave and wave setup measurements on shore platforms. We particularly formulate the following questions: What is the impact of platform roughness on wave dissipation and resulting mean circulation ? What are the subsequent effects on wave setup development ? To address these questions, wave transformation and wave setup dynamics are investigated on a gently sloping shore platform that extends in the nearshore subtidal zone. A first field campaign was carried out in fair weather conditions on the intertidal zone of the shore platform while a second one, more extensive, was conducted under storm wave conditions with instruments deployed from 10 m water depth up to the shoreline. Field data analysis is complemented with numerical simulations performed with a fully coupled (wave-current) 3D modeling system that uses a vortex force formalism. Based on the results, the relative importance of depth-induced breaking to wave bottom friction on the platform is examined. The effects of bottom roughness on the wave-induced circulation and wave setup dynamics are then analyzed, notably through additional numerical experiments with idealized shore platforms and sandy beaches of varying uniform slopes. After presenting the study area in Section 2, the modeling system is described in Section 3. The ability of the modeling system to simulate the transformation of short waves, water levels and mean current velocities over the considered shore platform is investigated in Section 4. In Section 5, the relative importance of short-wave dissipation by depth-induced breaking and bottom friction are discussed. The potential effects of bottom roughness affecting wave setup through wave dissipation and resulting circulation are then investigated, followed by conclusions in Section 6.

2. Study Area and Field Experiment

2.1. Study Area

The studied shore platform is located in the central part of the French Atlantic Coast along the Western coast of Oléron Island (Figure 1a). The coast in the region is bordered by a 150 km-wide shelf, which exhibits gently sloping shorefaces. According to Dodet et al. (2019), the tidal regime is semi-diurnal and macrotidal, with a tidal range varying from 1.10 to 5.50 m. These authors also analyzed wave regimes along the 30 m isobath line of the

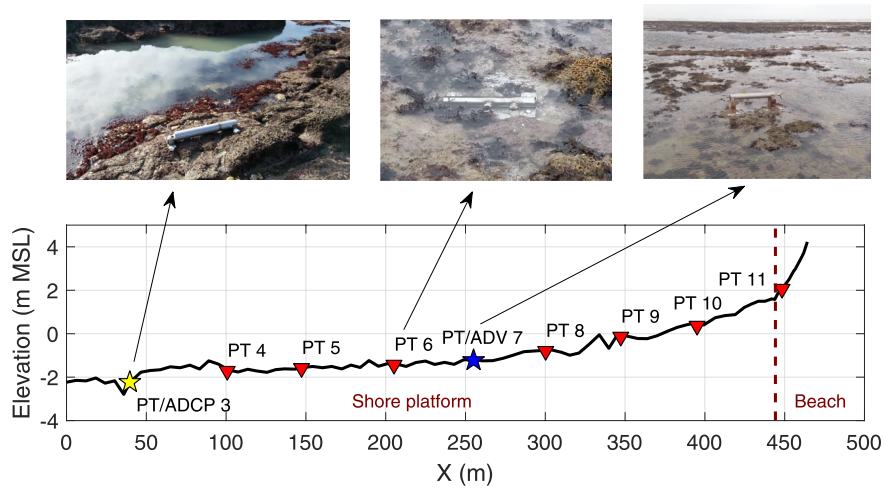

Figure 2. Cross-shore profile of the intertidal zone with location of the stations 3 to 11 deployed during storm wave conditions.

metropolitan coasts of France and reported in the region, yearly averaged significant wave height (hereafter H_{m0}) of 1.60 m and yearly averages of mean wave period and wave direction of 5.9 s and 275° respectively. Winter storms can however drive waves of H_{m0} over 10 m in the Bay of Biscay (Bertin et al., 2015).

The intertidal shore platform is 450 m-wide (full spring intertidal range), which corresponds to the upper range of platforms widths as compared to previously published studies on macrotidal platforms (Naylor & Stephenson, 2010; Poate et al., 2018; Stephenson et al., 2018). The platform is characterized by a very gentle slope of 1:250 increasing up to 1:50 at the top of the platform (x between 300 and 445 m, see Figure 2). The platform is a marl-limestone formation characterized by shallow steps and pools, except at the beginning of the profile (before $x = 50$ m) where steep pools (~1 m deep) can develop. At its landward edge (from $x = 445$ m), the platform is backed by a sandy dune with a steep sandy beach (slope of 1:10) at the platform-dune junction. At its seaward edge (before $x = 0$ m), the subtidal portion of the platform plunges into the sea with a slope of 1:65 before being more gently sloping, and extends until ~3,000 m offshore.

2.2. Field Experiments

Two field campaigns were conducted on the shore platform under contrasting wave-energy conditions. The first one was carried out on the intertidal part of the platform during one day (two tidal cycles) in March 2019, under spring tides with a 5.50 m tidal range and weak-energy wave conditions (hereafter referred to as fair weather conditions). Maximum significant wave height and peak period of 1.5 m and 15 s respectively, were recorded at the Datawell Oléron buoy (operated by CEREMA and located at a depth of 50 m; see Figure 1a for its location). A detailed description of this campaign and the associated results on short wave transformation using a simple energy flux model can be found in Lavaud, Pezerat, et al. (2020). Since this field experiment is characterized by small waves and low wind conditions, it is specifically used in the present study to investigate bottom friction effects on wave dissipation and in particular, to determine the roughness length k_n (see Section 3.2) of the platform through a sensitivity analysis of the model to this parameter. The second field campaign was conducted from 7 to 13 February 2020, under spring tides with a maximum tidal range of 5.20 m, and storm wave conditions (maximum significant wave height and peak period of ~6 m and 17 s respectively, recorded at Oléron buoy). This field campaign was more extensive than the first one, since it covered not only the intertidal zone but also the subtidal part of the platform. In the intertidal zone, a 400 m-long cross-shore transect was instrumented from 9 February with 7 pressure transducers (hereafter PT), a 2 MHz Acoustic Doppler Current Profiler (hereafter ADCP) and a 6 MHz Acoustic Doppler Velocimeter (hereafter ADV), both equipped with an internal PT (Figures 1c and 2). The instruments were spaced at 45 m intervals, allowing to cover most of the full spring intertidal zone, and were all housed in stainless steel tubes screwed to the bedrock (Figure 2), except the most landward PT (PT 11) which was fixed to a rock buried in 0.10 m of sand on the backing beach. However, this sensor was not considered in this analysis as it was located in the swash zone and hence, not continuously submerged. Also, pressure signals

recorded at PT 3 and 7 showed drifting and were therefore discarded from the analysis of water levels and wave setup. In the subtidal zone, a 600 kHz ADCP equipped with an internal PT (PT 1) and an additional PT aiming at identifying possible sensor drifting (PT 0, not shown) were deployed about 1,750 m offshore at a depth of approximately 9 m relative to mean sea level. Another single PT was deployed closer to shore, at 1,000 m in a depth of approximately 8 m relative to mean sea level (Figure 1b). Both subtidal stations were located on the shore platform, although PT 2 was deployed in a small sandy zone surrounded by the rocky bottom. The PTs of the overall deployment measured at 2 Hz except the internal PT of the ADV, which measured at 16 Hz.

Data from both field experiments were analyzed similarly, as described below. Bottom pressure measurements were first corrected for sea level atmospheric pressure measured at the nearby meteorological station of Chassiron (Figure 1a). Each data record was then analyzed using consecutive bursts of 30 min (20 min for the internal PTs of ADCPs). At each sensor located in the intertidal zone, bursts of mean water depth less than 0.50 m were discarded from this analysis as the sensors were intermittently dry due to the presence of fluctuations induced by infragravity waves. Hydrostatic surface elevation spectra were computed by averaging estimates from 10 Hanning-windowed segments overlapping by 50% (20 degrees of freedom). Correction for pressure attenuation with depth was done using a transfer function derived from linear wave theory (e.g., Bishop & Donelan, 1987). The significant wave height H_{m0} and mean wave period $T_{m0,2}$ were computed as:

$$H_{m0} = 4\sqrt{m_0} \tag{1}$$

$$T_{m02} = \sqrt{\frac{m_0}{m_2}} \tag{2}$$

where the 0th moment m_0 and 2nd moment m_2 were calculated with the following equation:

$$m_n = \int_{f_{\min}}^{f_{\max}} f^n E(f) df \tag{3}$$

In Equation 3, $E(f)$ is the surface elevation energy density spectra and the frequency cut off $f_{\max}$ is set to 0.3 Hz. The frequency cut off between short and infragravity waves $f_{\min}$ is adaptive and defined as $1/1.8T_p$ with T_p the continuous peak period recorded at Oléron buoy (Figure 1a), which follows the approach of Roelvink and Stive (1989), Oh et al. (2020), and Bertin et al. (2020).

In the subtidal zone, a high resolution (0.2×0.2 m regular grid) multibeam bathymetric survey was performed on approximately 1.73 km^2 to dispose of accurate bathymetric data of the study area. This high-resolution data set was also used to physically quantify the bottom roughness length k_n of the platform: it was estimated as four times the standard deviation of the bed elevation (Lowe et al., 2005; Poate et al., 2018) and was computed by averaging several estimates from 1 m^2 tiles across the platform, leading to an averaged value of 0.15 m. Bathymetric data of the intertidal zone originates from a LiDAR survey carried out in 2010 in the scope of the National Project LITTO3D (conducted by the National Geographic Institute and the French Navy). A GNSS receiver was also used to survey several cross-shore profiles of the intertidal shore platform at low tide, and measure the position of each sensor to calculate the wave setup. At the intertidal PTs (except stations 3, 7, and 11 discarded from this analysis), the wave setup was computed as the difference in mean free surface elevations η between each PT and the deepest one (PT 1), which requires an estimate of its vertical position (bathymetry) d not known in the field a priori ($h = d + \eta$ with h the mean water depth). For this, the calmest conditions of the experiment (high tide, wind velocity inferior to 5 m.s^{-1} and weak wave contribution) were carefully determined, such that the mean free surface elevation η can be assumed horizontal between PT 1 and PT 4 at this instance ($\eta_1 = \eta_2$ with η_2 known as d_2 was leveled in the field), and the vertical position of PT 1 can be estimated as $h_1 - \eta_1$ (see Appendix B). The wave setup was then calculated at each sensor except at PT 2, as this instrument progressively sank into the sand during the field campaign.

3. Modeling System

3.1. Overview of the Modeling System

This study uses the modeling system SCHISM (Semi-implicit Cross-scale Hydroscience Integrated System Model) of Zhang et al. (2016) which is a 3D unstructured-grid model, developed from the original model SELFE

(Zhang & Baptista, 2008). A combination of a semi-implicit scheme with an Eulerian-Lagrangian Method used to treat the momentum advection, allows to relax the numerical stability constraints. A detailed description of the model, its governing equations as well as its numerical implementation can be found in Zhang et al. (2015) and Zhang et al. (2016). The hydrodynamic model can be coupled with other models, all sharing the same unstructured grid and domain decomposition to limit the exchange of information between the models and avoid errors of interpolation. In this study, 3D fully coupled wave-current simulations are performed by coupling the hydrodynamic model to the spectral Wind Wave Model WWM of Roland et al. (2012). The effects of short waves on the mean circulation are represented with the vortex force formalism proposed by Bennis et al. (2011), which is based on glm2z-RANS theory (Ardhuin et al., 2008). Its original implementation in SCHISM is described in Guérin et al. (2018) (see Appendix A1 for the governing equations) while new developments related to the non-conservative wave effects are presented in Section 3.3. Also, further improvements on the modeling of the wave-induced turbulence at the surface are detailed in Appendix A3.

3.2. The Spectral Wave Model WWM

WWM simulates the generation and propagation of wind-generated waves by solving the wave action equation (e.g., see Komen et al. 1994). In this study, energy dissipation due to whitecapping and wind input are computed according to Bidlot et al. (2002), which corresponds to the ECMWF parameterization. Nonlinear wave-wave interactions in deep water (quadruplet interactions) and in shallow water (triad interactions) are calculated according to the Discrete Interaction Approximation of Hasselmann et al. (1985) and to the Lumped Triad Approximation of Eldeberky (1996) respectively. Wave energy dissipation by depth-induced breaking is computed following the approach of van der Westhuysen (2010) in which the local mean rate of energy dissipation per unit area reads:

$$D_{br} = \frac{3\sqrt{\pi}}{16} B^3 \rho g \frac{f_{mean}}{h} \left(\frac{\beta_i}{\beta_{i,ref}} \right)^n H_{rms}^3 \tag{4}$$

where B is the breaking coefficient of the order of 1, f_{mean} is the mean wave frequency computed from the $T_{m0,1}$ wave period, H_{rms} is the root-mean-square wave height $\left(H_{rms} = H_{m0}/\sqrt{2} \right)$, h is the mean water depth, g is the acceleration caused by gravity and ρ is the water density. β_i is the biphase, a third-order quantity related to the asymmetry of the wave profile. In WWM, the parametrization of Eldeberky (1996) is used to approximate the biphase as phase-averaged wave models do not compute quantities at this order. It reads:

$$\beta_i = \frac{-\pi}{2} + \frac{\pi}{2} \tanh \left(\frac{\delta}{U_r} \right) \tag{5}$$

where δ is a parameter set to 0.2 according to Eldeberky (1996). U_r is the Ursell number, computed following the spectral mean expression given by Eldeberky (1996):

$$U_r = \frac{g}{8\sqrt{2}\pi^2} \frac{H_{m0} T_{m0,1}^2}{h^2} \tag{6}$$

In Equation 4, $\beta_{i,ref}$ and n are coefficients set to $-4\pi/9$ and 2.5 respectively, which are the values used by van der Westhuysen (2010). In WWM, the source term due to depth-induced breaking is computed following the approach of Eldeberky and Battjes (1996):

$$S_{br}(\sigma,\theta) = -\frac{D_{tot}}{E_{tot}} N(\sigma,\theta) \text{ where } E_{tot} = \rho g \int_0^{2\pi} \int_0^{\infty} E(\sigma,\theta) d\sigma d\theta \tag{7}$$

where σ is the wave relative angular frequency and θ is the wave direction. E_{tot} and E are the total and spectral wave energy density respectively and $N = \rho g E/\sigma$ is the spectral wave action density.

Recently, Pezerat et al. (2021) reported that common parameterizations for depth-induced breaking in spectral wave models yield significant over-dissipation of storm waves propagating over gently sloping shorefaces, which can potentially lead to an underestimation of the wave setup at the shoreline. To overcome this problem, the authors proposed an adaptive parameterization of the breaking coefficient B based on the local bottom slope. In

this study, the formulation of van der Westhuysen (2010) is used with this adaptive parameterization of B, while comparisons with simulations using $B = 1$ are conducted in Section 4.1.2.

Finally, the source term due to bottom friction is expressed as:

$$S_{bf}(\sigma,\theta) = -C_f \frac{\sigma^2}{g^2 \sinh^2(k(\sigma)h)} N(\sigma,\theta) \tag{8}$$

where k is the wavenumber computed with the linear dispersion relation and C_f is a dissipation coefficient (in $m^2 \cdot s^{-3}$) calculated according to the eddy-viscosity model of Madsen et al. (1989):

$$C_f = \frac{g}{\sqrt{2}} f_w U_{rms} \tag{9}$$

where U_{rms} is the root-mean-square bottom-orbital velocity and f_w is a non-dimensional frictional factor expressed as a function of the near-bottom excursion amplitude and the Nikuradse roughness length k_n according to Jonsson (1967). The default value for k_n in WWM is 0.05 m, which relates to a sandy bottom with bedforms. The spatial distribution of bottom types, and in particular the extension of the studied rock platform, is here based on the sediment database of the SHOM (French Naval Oceanographic Service). Considering the direct estimates of k_n made from the high-resolution multibeam bathymetric survey (see Section 2.2), the value of k_n was then adjusted by minimizing the discrepancies between model predictions and observations during fair weather conditions (see Section 4.1.1). Outside of the rocky area, k_n is set to its default value 0.05 m. In order to evaluate the influence of the bottom friction formulation on the performance of the model, simulations were also carried out with the Madsen's formulation using a uniform k_n set to 0.05 m, and with the widely used JONSWAP formulation of Hasselmann et al. (1973), based on a friction coefficient C_f spatially uniform and fixed to the empirical value of 0.038 $m^2 \cdot s^{-3}$.

3.3. Non-Conservative Wave Accelerations

The vortex force formalism decomposes wave forces into conservative (i.e., vortex force and wave-induced mean pressure, see Appendix A1) and non-conservative forces, where the latter correspond to accelerations induced by wave dissipation processes. The modeling system accounts for accelerations due to depth-induced breaking as described in Guérin et al. (2018), and accelerations owing to energy dissipation by whitecapping and bottom friction which have been implemented more recently.

Within the surf zone, a fraction of wave energy dissipated by wave breaking is converted into surface rollers. Besides contributing to the mass transport in the surf zone (Svendsen, 1984), surface rollers induce a lag in the transfer of momentum to the water column by modifying the spatial distribution of breaking accelerations (e.g., over bars, see Reniers et al., 2004). In order to account for this effect, a model of surface rollers following Reniers et al. (2004) has been implemented in WWM with minor adjustments (see Appendix A2). Accelerations due to depth-induced breaking, whitecapping and surface rollers are gathered in a single term expressed as follows:

$$\left(\hat{F}_{br,x}(z), \hat{F}_{br,y}(z)\right) = \frac{f_{br}(z)}{\rho} \left(- \int_0^{2\pi} \int_0^{\infty} (\cos\theta, \sin\theta) k(\sigma) \left((1-\alpha_r) S_{br}(\sigma,\theta) + S_{ds}(\sigma,\theta)\right) d\sigma d\theta + (\cos\theta_m, \sin\theta_m) \frac{k_p}{\sigma_p} D_{rol} \right) \tag{10}$$

where α_r is the percentage of energy transferred from breaking waves to surface rollers. Here, we assume a full conversion of energy from breaking waves to surface rollers with $\alpha_r = 1$, as it leads to the best predictions of wave setup. D_{rol} corresponds to the rate of surface roller energy dissipation (see Appendix A2), and the subscripts "m" and "p" refer to the mean and peak value of the corresponding wave parameter, respectively. $f_{br}(z)$ corresponds to an empirical vertical distribution function which can be defined with different expressions (Uchiyama et al., 2010). In this study, $f_{br}(z)$ is defined such that accelerations by breaking-induced processes are applied in the surface layer (Guérin et al., 2018), which is similar to representing them as surface stresses (Deigaard, 1993).

In intermediate to shallow water depths, the wave energy dissipated by bottom friction within the wave boundary layer induces a near-bottom current in the direction of wave propagation referred to as wave streaming (Longuet-Higgins, 1953). The acceleration owing to wave bottom streaming is computed as follows:

$$\left(\hat{F}_{bot,x}(z), \hat{F}_{bot,y}(z)\right) = -\frac{f_{bot}(z)}{\rho}\int_0^{2\pi}\int_0^{\infty}(\cos\theta, \sin\theta)\, k(\sigma) S_{bot}(\sigma,\theta) d\sigma d\theta \tag{11}$$

The streaming acceleration is assumed to decrease upward across the wave boundary layer according to the vertical function $f_{bot}(z)$ (Uchiyama et al., 2010) given by:

$$f_{bot}(z) = \frac{1-\tanh(k_{wd}(z+d))^2}{\int_{-d}^{\eta} 1-\tanh(k_{wd}(z+d))^2 dz} \tag{12}$$

where d is the bathymetry ($h = d + \eta$ with η the mean free surface elevation) and $k_{wd} = 1/(a_{wd}\delta_{wd})$ is a decay length in which δ_{wd} is the wave bottom boundary layer thickness computed according to Fredsøe and Deigaard (1992):

$$\delta_{wd} = 0.09\left(30 z_0^{bot,w}\right)\left(\frac{A_{orb}}{30 z_0^{bot,w}}\right)^{0.82} \tag{13}$$

with A_{orb} the near-bottom excursion amplitude and $z_0^{bot,w}$ the apparent bottom roughness length under the combined effects of waves and currents (see Section 3.4). With $a_{wd} = 1$, we retrieve the theoretical thickness of the wave bottom boundary layer under monochromatic waves. In the present study, a_{wd} is fixed to 5, which is discussed in Section 5.2.

3.4. Bottom and Surface Stresses Parameterizations

At the surface, the wind stress is commonly parameterized with a bulk formula of the form $\rho_a C_d U_{10}^2$, where ρ_a is the air density, U_{10} is the wind speed at 10 m height above the sea surface and C_d is a drag coefficient usually computed as a linear function of U_{10} (i.e., Pond & Pickard, 1983). However, several studies reported that the sea surface roughness z_0 also varies with the sea state (Donelan et al., 1993; Mastenbroek et al., 1993). A younger sea state induces a rougher sea surface and hence increases the surface stress. It is expected to occur in the shoaling zone, where the wavelength decreases, enhancing the sea surface roughness. To account for this process in circulation models, several authors proposed to relate the surface roughness to wave parameters such as the wave age (Donelan et al., 1993) or the wave-induced stress (Janssen, 1991). In this paper, the formulation proposed by Donelan et al. (1993) is used to compute z_0:

$$\frac{z_0}{H_{rms}} = 6.7.10^{-4}\left(\frac{U_{10}}{c_p}\right)^{2.6} \tag{14}$$

where H_{rms} and c_p, the wave phase speed corresponding to the peak frequency, are provided by the wave model. The surface stress is obtained after computing C_d with the relationship $\sqrt{C_d} = \kappa/\log(z_{obs}/z_0)$ where κ is the von Kármán's constant ($\kappa = 0.4$) and z_{obs} is the height at which the wind is taken ($z_{obs} = 10$ m).

At the bottom, the model of Soulsby (1997) is used to compute the bottom stress under the combined action of waves and currents. This wave-current bottom stress τ_{wc} and apparent roughness length $z_0^{bot,w}$ are then used in the boundary condition for the turbulent kinetic energy (TKE) in the turbulence closure model (see Appendix A3).

3.5. Model Implementation

The unstructured computational grid used in the hindcast of the field experiments extends over the Pertuis Charentais area (Figure 1a), from the land boundary to ~73 km offshore corresponding to a depth of 90 m. Such a large extent is necessary to realistically reproduce the generation and propagation of storm surges over the continental shelf (Blain et al., 1994; Oliveira et al., 2020). The grid has ~76,000 nodes in the horizontal, with a spatial resolution ranging from 1,800 m along the open boundary to 10 m along the shoreline in the study area. Such a fine resolution is required to capture the wave-induced setup that develops along the shoreline (Lavaud, Bertin, et al., 2020). In the vertical, the grid is discretized in 24 terrain-following S-layers that are denser close to the bottom and surface.

The circulation model is forced at its open boundary with the 16 main astronomical constituents linearly interpolated from the regional model of Bertin et al. (2012). The bottom roughness length z_0^{bot} in the circulation model is spatially variable to account for the different bottom types in the modeled domain. After a sensitivity analysis (see Section 4.2), z_0^{bot} was set to 0.0001 m in sandy areas and to 0.02 m on the studied shore platform and other rocky bottoms. The hydrodynamic time step is set to 15 s while the wave model is run every 60 s and uses implicit schemes for propagation and source term integration (Roland et al., 2012).

Over the whole domain, the circulation model is forced with hourly 10 m wind speed U_{10} and sea-level pressure fields from the Climate Forecast System Reanalysis CFSR (Saha et al., 2010). The datasets are provided on a regular grid with a spatial resolution of 0.2° and 0.5° for the wind and the atmospheric pressure respectively. WWM is forced with CFSR wind fields over the whole domain and time series of directional wave spectra along its open boundary, which were previously computed from a regional application of the WAVEWATCH III spectral wave model also forced with wind fields from CFSR.

4. Results

In this section, we assess the ability of the modeling system to reproduce the observed water levels, the transformation of short waves and the associated circulation over the shore platform. Modeled wave parameters are first compared against field observations collected during fair weather conditions in order to determine the Nikuradse roughness length k_n that characterized the platform. Indeed, at high tides during this period, waves are predominantly dissipated by bottom friction on a large portion of the intertidal shore platform as the surf zone is located very close to the shoreline, making this period particularly suitable for analyzing wave bottom friction dissipation and the sensitivity of the model to k_n. The value of k_n yielding the best-fit results is then used in the simulation of storm wave conditions, from which short waves, currents and wave setup predictions are examined. Model errors are quantified by computing for each variable, the bias, the Root-Mean-Square Error (hereafter RMSE) and the NRMSE, which corresponds to the RMSE normalized by the mean of the observations.

4.1. Wave Predictions

4.1.1. Fair Weather Conditions

During the 1-day field campaign conducted in fair weather conditions, offshore significant wave height H_{m0} varied between 1.1 and 1.5 m at Oléron buoy (see Figure 1a for its location), which is well predicted by the model with a RMSE of 0.09 m, yielding a NRMSE of 7% (not shown). Figure 3b compares at the second high tide the cross-shore evolution of H_{m0} measured, and modeled with different bottom friction formulations. At this tidal stage (water depth of 4.50 m at the offshore sensor, see Figure 3a), the surf zone is relatively narrow and starts approximately at $x \sim 225$ m, implying that wave dissipation at the three most offshore sensors principally occurs through bottom friction. The data at these cross-shore locations are hence suitable to calibrate the Nikuradse roughness length in the Madsen's formulation. The sensitivity analysis to this parameter revealed that the value of $k_n = 0.13$ m taken on the platform (and 0.05 m outside, see Section 3.2) best reproduces the observed wave height at the three offshore sensors with a RMSE of 0.023 m. Keeping the default value $k_n = 0.05$ m uniform over the whole computational domain (model 2 in Figure 3b) or using the JONSWAP bottom friction formulation with $C_f = 0.038$ m^2·s^{-3} (model 3 in Figure 3b) leads to an underestimation of wave frictional dissipation with RMSE of 0.11 and 0.26 m respectively. Based on these results, the Madsen's formulation with k_n set to 0.13 m on the platform was used in the hindcast of the second field campaign conducted in storm wave conditions.

4.1.2. Storm Wave Conditions

As in fair weather conditions, simulated offshore wave parameters are compared against measurements recorded at Oléron buoy (Figure 1a). The comparison reveals a very good agreement between observed and modeled significant wave height H_{m0} with a RMSE of 0.26 m which corresponds to a 6% NRMSE. The mean wave period T_{m02} was of the order of 8–10 s and the peak period T_p varied between 13 and 17 s during the field campaign, which is well reproduced by the model with RMSE of ~0.40 and 0.50 s respectively, corresponding to NRMSE less than 5%. The peak direction P_{dir} is also well predicted by the model with a RMSE of 6°. It is worth noting that H_{m0} reached almost 6 m during the field campaign, a value reached 5 times since January 2020, therefore corresponding to energetic but not exceptional winter conditions (Figure 4).

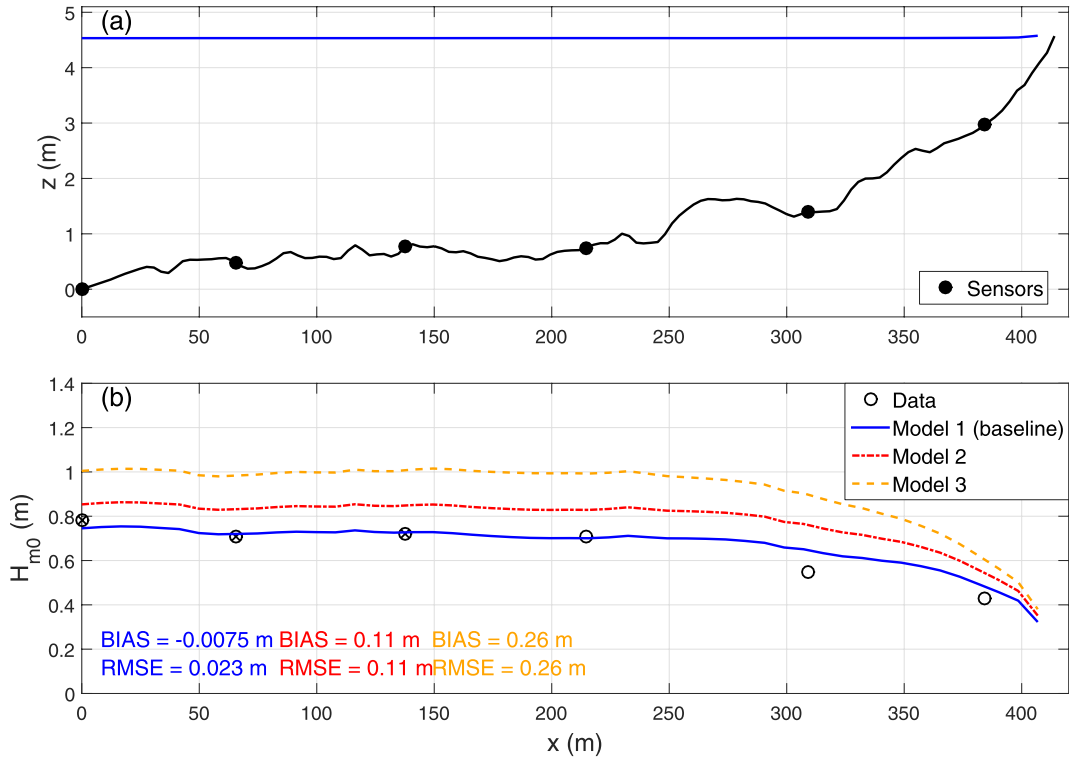

Figure 3. (a) Bathymetry (black line) and mean free surface elevation (blue line) along the intertidal transect instrumented in fair weather conditions (both are given relative to the bathymetric elevation of the first sensor) and (b) observed (black dots) against significant wave height H_{m0} modeled with the baseline model using Madsen's formulation with $k_n = 0.13$ m for rocky areas and 0.05 m outside (model 1), the model using the Madsen's formulation with k_n set uniform to the default value 0.05 m (model 2) and the model using the JONSWAP formulation with $C_f = 0.038$ m^2·s^{-3} (model 3), at the second high tide along the transect. The black crosses correspond to where statistical errors are computed (RMSE, BIAS).

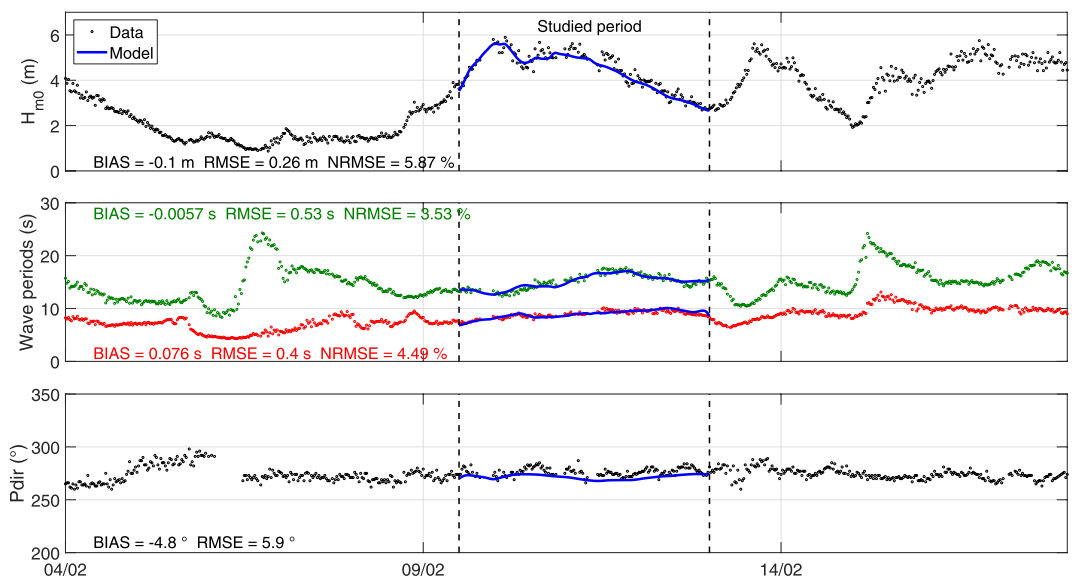

Figure 4. Assessment of the model at the offshore Oléron buoy with comparisons of the modeled (blue line) against observed significant wave height H_{m0}, peak direction P_{dir} (black dots), mean wave period $T_{m0,2}$ (red dots) and peak period T_p (green dots).

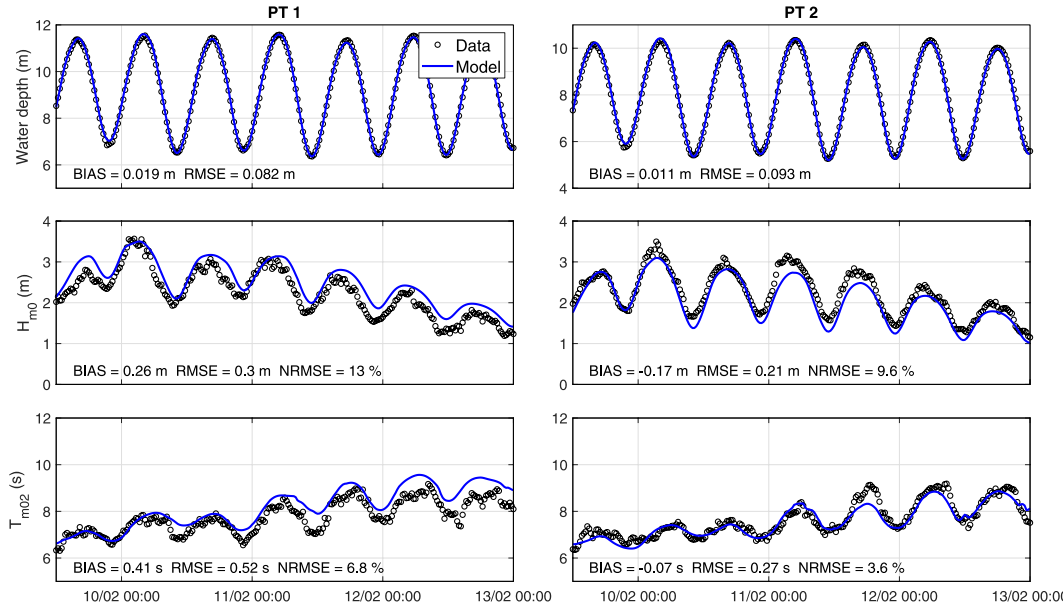

Figure 5. Assessment of the model at the subtidal sensors (PT 1 and PT 2) with comparisons of the modeled (blue line) against observed water depth, H_{m0} and $T_{m0,2}$ (black dots).

In the nearshore region, the water levels at PT 1 and PT 2 are well reproduced by the model with RMSE of 0.08–0.09 m (Figure 5). At both sensors, H_{m0} is tidally modulated with H_{m0} decreasing as the water depth decreases, suggesting that wave breaking is already significant at these depths. Maximum H_{m0} values were measured at PT 1 in the morning of 10/02 at high tide, with a value of 3.60 m for a corresponding mean wave period T_{m02} of ~7.5 s. At PT 1, H_{m0} is predicted relatively accurately with RMSE of 0.30 m, yielding a 13% NRMSE although H_{m0} is slightly over-estimated during the whole period with a positive bias of 0.26 m. At PT 2, H_{m0} is well predicted by the model with a NRMSE of 9.6%. Mean wave periods T_{m02} are slightly over-estimated at PT 1 with a positive bias of ~0.40 s, while at PT 2, it is accurately reproduced by the model with a NRMSE of 3.6%. Similar to the significant wave height, T_{m02} also exhibits a tidal modulation at both sensors, which is slightly more pronounced at PT 2, with T_{m02} being smaller at low tides by up to 2 s. When the triad interactions source term is turned off in the simulation, the wave period exhibits an inverse and weaker tidal modulation, revealing that the observed tidal modulation is due to triad interactions in shallow waters. At a given sensor, more energy is transferred from the primary peak to super harmonics as the water depth decreases, explaining the lower wave period.

As a general trend, wave heights in the intertidal zone (Figures 6b–6g) are highest at the most seaward sensor (PT 4) and decrease across the platform toward the shoreline. At the first sensor in the intertidal zone (PT 4, Figure 6b), the wave height is depth-limited over the first six tidal cycles. Over the last one, the same behavior can be observed from low to mid tidal stages while from mid to high tidal stages, the wave height does not increase when the water depth increases (water depth at PT 1, Figure 6a), suggesting that this sensor was located outside the surf zone. At the landward sensors (from PT 5 to PT 10; Figures 6c–6g), short waves are depth-limited during the whole period, so that they were always located in the surf zone. The comparison with the model shows that wave heights at all stations are well predicted by the model with NRMSE ranging from 8% to 14%. In more details, H_{m0} is slightly underestimated by 0.15–0.20 m at PT 9 and 10 at high tides over the last 2 days of the experiment, which is possibly due to wave reflection on the 1:10 sloping beach, a process not represented in the model. Note that using a default parameterization for depth-induced breaking ($B = 1$), wave predictions considerably deteriorate at PT 2 (negative bias of 0.60 m and NRMSE of 30%) and in the intertidal zone with a negative bias of 0.40 m resulting in a NRMSE of 43% in average (not shown). On the contrary, using a default parameterization for bottom friction (JONSWAP formulation with $C_f = 0.038$ m^2·s^{-3}) results in positive bias of 0.70 and 0.17 m and NRMSE of 30% and 20% in average, at the sensors of the subtidal and intertidal zones respectively (not shown). The importance of accurately representing short-wave dissipation on wave setup is shown in Section 4.3.

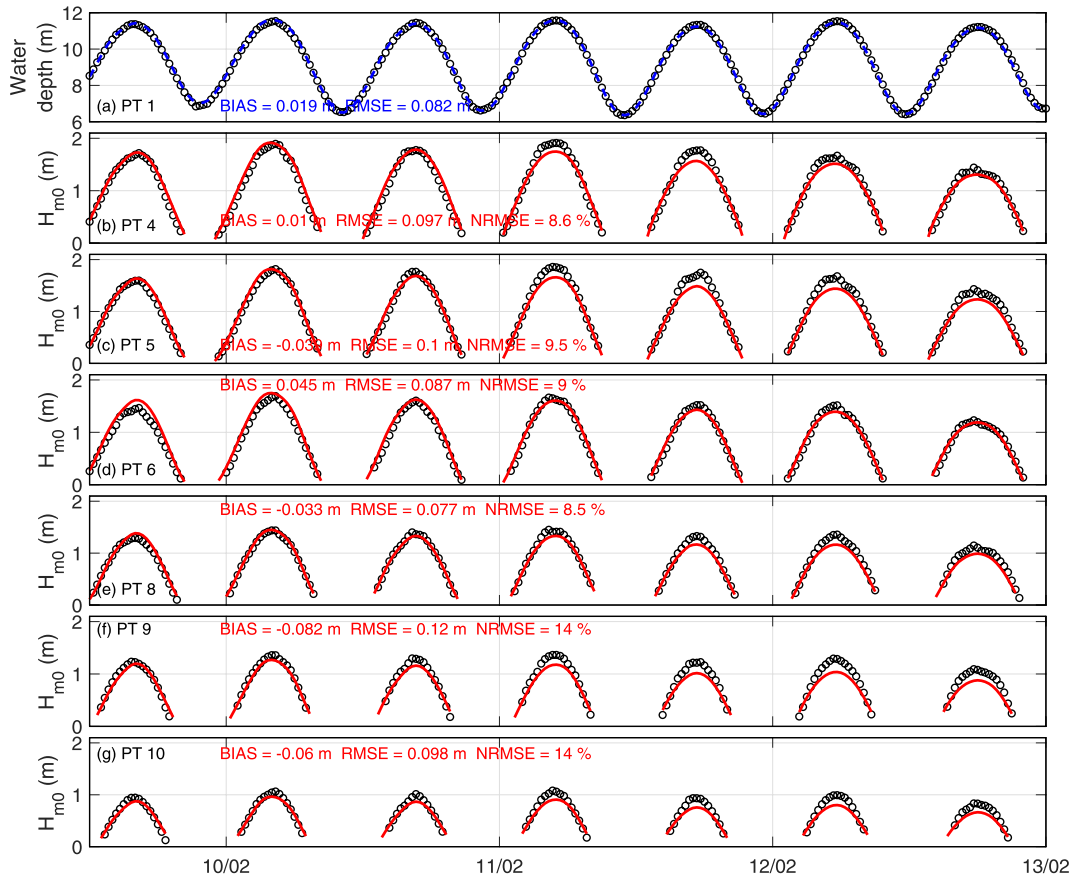

Figure 6. Modeled (blue line) against observed water depth at the subtidal sensor PT 1 (panel a) and assessment of the model at the intertidal sensors (from PT 4 to PT 10) with comparisons of the modeled (red line) against observed H_{m0} (black dots) (panels b to g).

4.2. Cross-Shore and Long-Shore Currents

The ability of the model to reproduce mean currents is assessed through a comparison with currents measured at the ADV (corresponding to PT 7 location), located at a height of 0.25 m above the seabed. The use of the ADCP in the surf zone provided incoherent patterns, possibly owing to the presence of air bubbles in the wave column affecting or even blocking the acoustic signal, which did not allow to analyze mean currents at this location. At the ADV, measured velocities and modeled quasi-Eulerian velocities at 0.25 m above the bed (vertical position of the ADV) were time-averaged over bursts of 20 min. The measured cross-shore velocity is always seaward-oriented, which suggests the presence of an undertow, reaching up to -0.20 m·s^{-1} (Figure 7b). Also, a slight asymmetry can be observed between flood and ebb in the measured cross-shore velocity, which suggests the influence of tidal currents (Figures 7a and 7b). The negative values of the longshore velocity, up to -0.12 m·s^{-1} indicate the presence of a weak longshore drift to the South-East of Oléron Island (Figure 7c). As in previous studies (Longuet-Higgins, 1970a, 1970b; Thornton & Guza, 1986), the reproduction of longshore currents is very sensitive to z_0^{bot}. Best agreements in longshore currents between the model and the measurements were obtained with $z_0^{bot} = 0.02$ m (RMSE of 0.030 m·s^{-1}), while halving this value yields an error twice as large. Predictions of the cross-shore velocity depart more from the measurements, mostly owing to a negative bias of 0.06 m·s^{-1} with local underestimations up to 0.10 m·s^{-1} (Figure 7b), yielding a RMSE of 0.064 m·s^{-1}.

4.3. Storm Surge and Wave Setup Predictions

Figure 8 presents modeled against observed surges at the different intertidal stations. Similar to the surge computed from the measurements, the modeled surge was calculated as the difference between mean free surface elevations at each PT in the intertidal zone and the most seaward sensor (PT 1). The modeled and observed surges

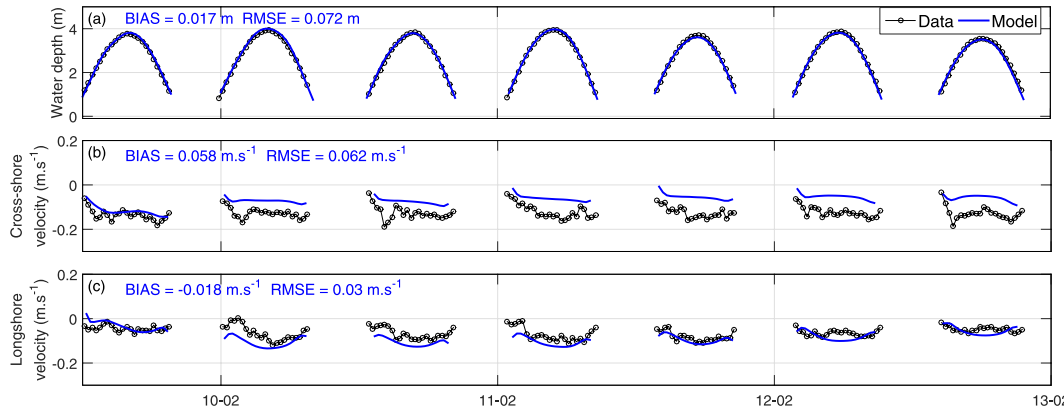

Figure 7. (a) Water depth at PT 6. Measured (b) cross-shore and (c) longshore currents (black dots) against modeled quasi-Eulerian velocities (blue line) at the vertical position of the ADV (0.25 m above the bed, PT 7 location).

comprise the wave setup and a part of the wind-induced surge that developed from PT 1 to the shoreline. According to the model results, the atmospheric surge ranged from 0.00 to 0.03 m most of the time during the field campaign but could reach up to 0.06 m at low tide during episodic strong wind events of up to 15 m·s^{-1} recorded at the meteorological station of Chassiron (see Figure 1a for its location). Besides this effect, the surge was mainly

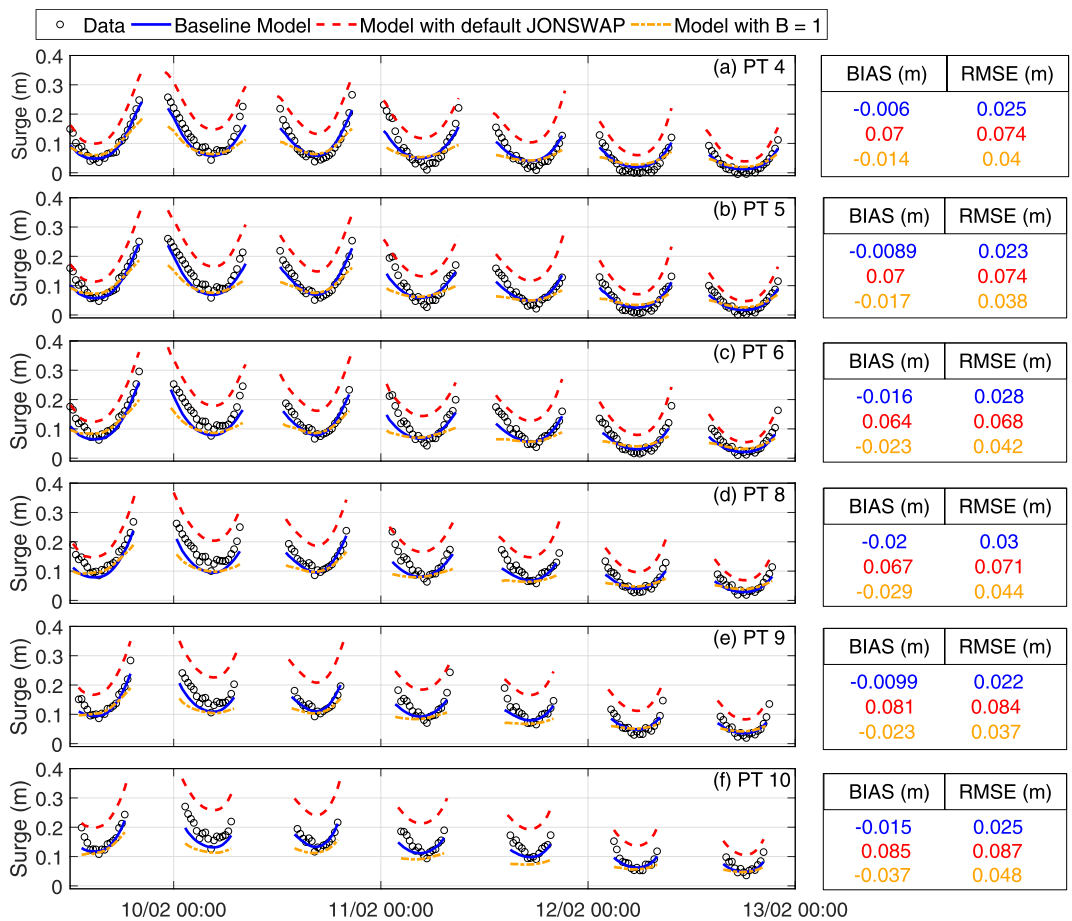

Figure 8. Observed (black dots) against modeled storm surges with the baseline model (blue line), with the default JONSWAP formulation (red dashed line) and with $B = 1$ in the depth-induced breaking formulation (orange dashed dotted line), at the intertidal PTs.

due to the wave setup, representing at least 80% of the surge. The measured surge reached up to 0.30 m at low tide during energetic wave conditions in the evening of 9 February. The comparison between the surge measured and simulated with the baseline model shows a relatively good agreement with RMSE of the order of 0.02–0.03 m for all the PTs. In more details, the model displays local underestimations of up to 0.08 m at certain low tides. In comparison, the model using a default parameterization for depth-induced breaking ($B = 1$) results in an underestimation of the wave setup at the water line, with negative bias up to 0.04 m at PT 10 and RMSE increased by 50%–90% compared to our baseline model (Figure 8). In line with the findings of Pezerat et al. (2021), our results show that the adaptive approach for the breaking coefficient proposed by these authors (see Section 3.2) strongly improves wave height and subsequently, wave setup predictions.

Regarding frictional effects, the use of the default JONSWAP bottom friction formulation ($C_f = 0.038$ m^2·s^{-3}) leads to a wave setup overestimated at all sensors in the intertidal zone with a positive bias of 0.065–0.085 m and RMSE 2 to 4 times larger compared to our baseline model (Figure 8). With our baseline model, the strong frictional effects that occurred on the platform seaward of the surf zone are correctly represented. Therefore, more wave energy is dissipated before wave breaking which modifies wave accelerations and results in a decreased wave setup, a process already shown in coral reef environments (Buckley et al., 2016; Lowe et al., 2009).

5. Discussion

The modeling results presented above demonstrate that the model can provide an accurate representation of short-wave dissipation and associated wave setup on the shore platform. In the present section, we thus use the modeling results to conduct detailed analyses of these processes.

5.1. Relative Importance of Wave Breaking to Frictional Dissipation on the Platform

The accurate representation of short-wave energy dissipation has required the use of adapted parameterizations of wave breaking and wave bottom friction. In particular, wave bottom friction in the model must account for the bottom roughness of the platform, which here corresponds to the Madsen's formulation with a Nikuradse roughness length $k_n = 0.13$ m. This value is comparable to the values of 0.10 m used by Delpey et al. (2014) and 0.12 m used by Roland and Ardhuin (2014) to represent rocky bottoms in their modeling systems. This value is also close to the platform roughness length of 0.15 m obtained from our centimeter-scale bathymetric survey (see Section 2.2). The latter value is in the range of the values measured by Poate et al. (2018) on contrasting shore platforms (0.07–0.17 m).

The importance of wave breaking and wave bottom friction processes is analyzed by calculating rates of wave energy dissipation D_{bf}/ρ and D_{ff}/ρ along a cross-shore profile at high tide during both fair weather and storm wave conditions (Figure 9). D_{bf}/ρ and D_{ff}/ρ are then integrated along the cross-shore profile to analyze their relative contribution to the total wave dissipation. In both contrasting wave energy conditions (fair weather/storm), the analysis reveals that wave energy dissipation is dominated by bottom friction outside the surf zone. In more details, during fair weather conditions, bottom friction occurring on the subtidal part of the platform and on a major part of the intertidal region accounts for 50% of the total wave energy dissipation, before wave breaking becomes the leading process of dissipation in the surf zone located very close the shoreline (from $x = 1{,}500$ m, Figure 9e). In storm wave conditions, wave breaking occurs locally in the subtidal zone but with dissipation rates weaker than bottom friction, the latter in this region representing ~25% of the total wave energy dissipation (from $x = 0$ to $x = 1{,}100$ m, Figures 9f and 9h). Similarly, Gon et al. (2020) reported that 32% of wave energy was dissipated by bottom friction on the inner self of a rocky shore. These frictional effects occur over distances less than 130 m, hence much shorter than the width of the subtidal platform here (≫1,000 m), but the rocky shore was characterized by a roughness length approximately 30 times higher than the one of the platform. Closer to shore and in the intertidal zone of the platform, wave breaking mostly dominates the dissipation, particularly when the bottom slope increases from $x = 1{,}100$–$1{,}400$ m with a maximum dissipation rate 8 times larger compared to bottom friction (Figure 9f). This zone is very effective in dissipating wave energy through wave breaking, acting similarly to the sharp seaward edge that characterized near-horizontal platform in micro-tidal settings (Ogawa et al., 2011). Overall, it should be noted that bottom friction across the entire platform represents approximately 50% and 42% of the total wave energy dissipation in fair weather and storm wave conditions respectively (Figures 9g and 9h). The latter represents significant dissipation effects as the total wave

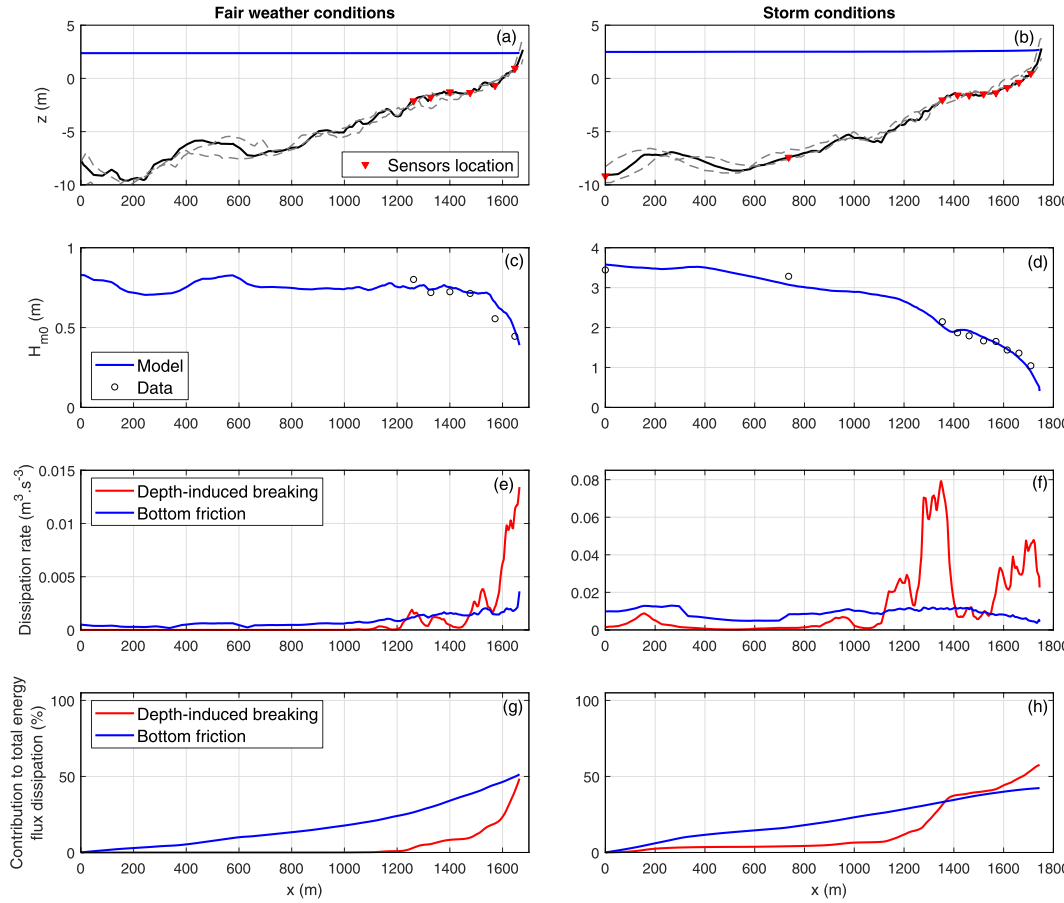

Figure 9. (a and b) Water levels, (c and d) H_{m0}, (e and f) rates of wave energy dissipation by depth-induced breaking and bottom friction normalized by the water density, and (g and h) their contribution to total wave energy flux dissipation along the transect from the subtidal to the intertidal zone, in fair weather and storm wave conditions. The instrumented transects during the two field campaigns were not exactly the same (200 m spacing), explaining the differences observed in the bathymetry (black lines in (a) and (b)). The gray dotted lines correspond to two transects at 100 m on both sides of the instrumented transects, which shows the alongshore non-uniformity on the bathymetry of the platform.

energy dissipated under storm wave conditions is large. In their analysis, Poate et al. (2018) found that bottom friction is negligible in the surf zone of these environments, being only important outside the surf zone for very rough, low-gradient platforms, during small wave conditions. Hence, they suggested that for the majority of Type A shore platforms, bottom friction could be discarded when investigating short wave transformation. While the dominance of wave breaking dissipation in the surf zone is also observed in our study, high frictional dissipation occurs in the subtidal part of the platform during storm wave conditions, which significantly decreases wave height before wave breaking. This notable effect of platform roughness on wave dissipation was not reported by Poate et al. (2018), as they instrumented intertidal shore platforms only. In addition to bottom friction, the complex nearshore bathymetry can enhance shallow-water processes such as refraction and diffraction (Kowalczyk, 2016; Marshall & Stephenson, 2011; Stephenson & Kirk, 2000), which also control wave energy that reaches the intertidal zone of the platform.

5.2. Effect of Wave Bottom Friction on the Mean Circulation

Wave dissipation by friction at the bottom also affects the nearshore circulation through the generation of a near-bottom streaming along the wave propagation direction (Longuet-Higgins, 1953). Wang et al. (2020) suggested that a high bottom roughness, which enhances the dissipation of short waves by bottom friction, can result in a stronger bottom streaming that can weaken the undertow close to the surf zone. A similar behavior was observed in our study, in which both the undertow and the wave setup were found to be sensitive to the vertical

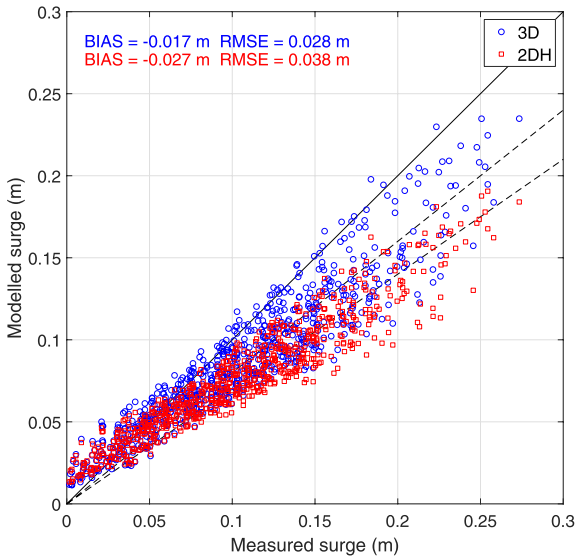

Figure 10. Observed against modeled surges with a 3D (blue circles) and a 2DH simulation (red squares). The dashed lines correspond to the 0.8:1 and 0.7:1 lines.

distribution of the bottom streaming (Equation 12), and particularly to the decay length k_{wd}. While k_{wd} with a_{wd} taken to 1 corresponds to the theoretical thickness of the turbulent wave bottom boundary layer, the laboratory experiments of Klopman (1994) suggest that a_{wd} can significantly increase under random waves. A value of 5 for a_{wd} was here retained, which is close to the value of 3 used by Reniers et al. (2004). Taking such a small value of a_{wd} may excessively reduce the undertow in the surf zone, which could partly explain the underestimated cross-shore current velocities at the ADV (Figure 7b). This hypothesis was verified by running the model with a uniform vertical distribution of the bottom streaming acceleration, which indeed increased the undertow and almost canceled out the remaining bias in the wave setup. The present approach to represent the effects of the bottom streaming on the nearshore circulation follows Uchiyama et al. (2010) and is based on theoretical analyses for progressive waves propagating in deep to intermediate water depths. However, several studies reported that the bottom streaming is reduced under asymmetric oscillatory flows (e.g., nonlinear waves) and can even become offshore-directed (Kranenburg et al., 2012; Trowbridge & Madsen, 1984; Xie et al., 2021). Hence, the present modeling approach of the bottom streaming might not be adapted in the surf zone, which is characterized by strongly asymmetric flows. Further research is needed to better understand the contribution of the bottom streaming to the surf zone mean circulation, and in particular, the vertical distribution of the associated acceleration should be verified. Other potential processes might also contribute to the discrepancy between modeled and measured cross-shore current at the ADV. The latter exhibits an asymmetric form between flood and ebb, suggesting the presence of tidal currents in addition to the undertow. A detailed inspection of the intertidal zone indicates that the rock topography is very complex, likely driving specific patterns of tidal-induced currents and locally forcing rip currents of small amplitude. In addition, the ADV location is surrounded by topography features of the same order of magnitude than the setting height of the ADV (0.25 m from the bed; see the photo of the ADV site, Figure 2), locally affecting the circulation. However, this topography is not well represented with the 10 m grid resolution, possibly explaining a limited prediction of these processes.

5.3. Effect of the Wave-Induced Mean Circulation on Wave Setup

Several studies showed that the wave setup near the shoreline does not only result from wave dissipation but can also be increased by the wave-driven, depth-varying circulation in the surf zone of sandy beaches (Apotsos et al., 2007; Guérin et al., 2018) or alongshore-uniform fringing reefs (Buckley et al., 2016). On sandy beaches, Guérin et al. (2018) suggested that the wave-driven circulation could have a larger contribution to the wave setup when the bottom slope increases. A similar trend is expected to occur on shore platforms, although the presence of a rougher bottom could result in substantial differences compared to the mechanisms identified by Guérin et al. (2018). To investigate this process, the wave setup obtained with our 3D baseline model is first compared to the one obtained with a 2DH simulation using the radiation-stress formalism of Longuet-Higgins and Stewart (1964), which does not represent the depth-varying circulation induced by waves (Figure 10). To perform a consistent comparison between 3D and 2DH simulations, the bottom drag coefficient is computed similarly using the formulation of Bretschneider et al. (1986) as in Zheng et al. (2013). The comparison reveals that the wave setup predictions are improved with the 3D simulation with a RMSE reduced by 26% and up to 30% for values of wave setup superior to the 90th percentile (Figure 10). These results suggest a non-negligible contribution of the wave-induced circulation to the wave setup.

To understand the underlying mechanisms of this contribution, an analysis of the 3D cross-shore momentum balance is conducted. The complex topography (i.e., subtidal rocky shoals and alongshore non-uniformity of the bathymetry, see cross-shore transects on Figures 9a and 9b) of our study site induces locally strong longshore advection that can contribute to the wave setup and which are represented in both the 2DH and 3D simulations. To discard these effects unrelated to 2DH/3D differences and also the non-stationarity of the wave, tide and wind forcings, we apply the 3D model to idealized cases with an alongshore uniform bathymetry. Six simulations are

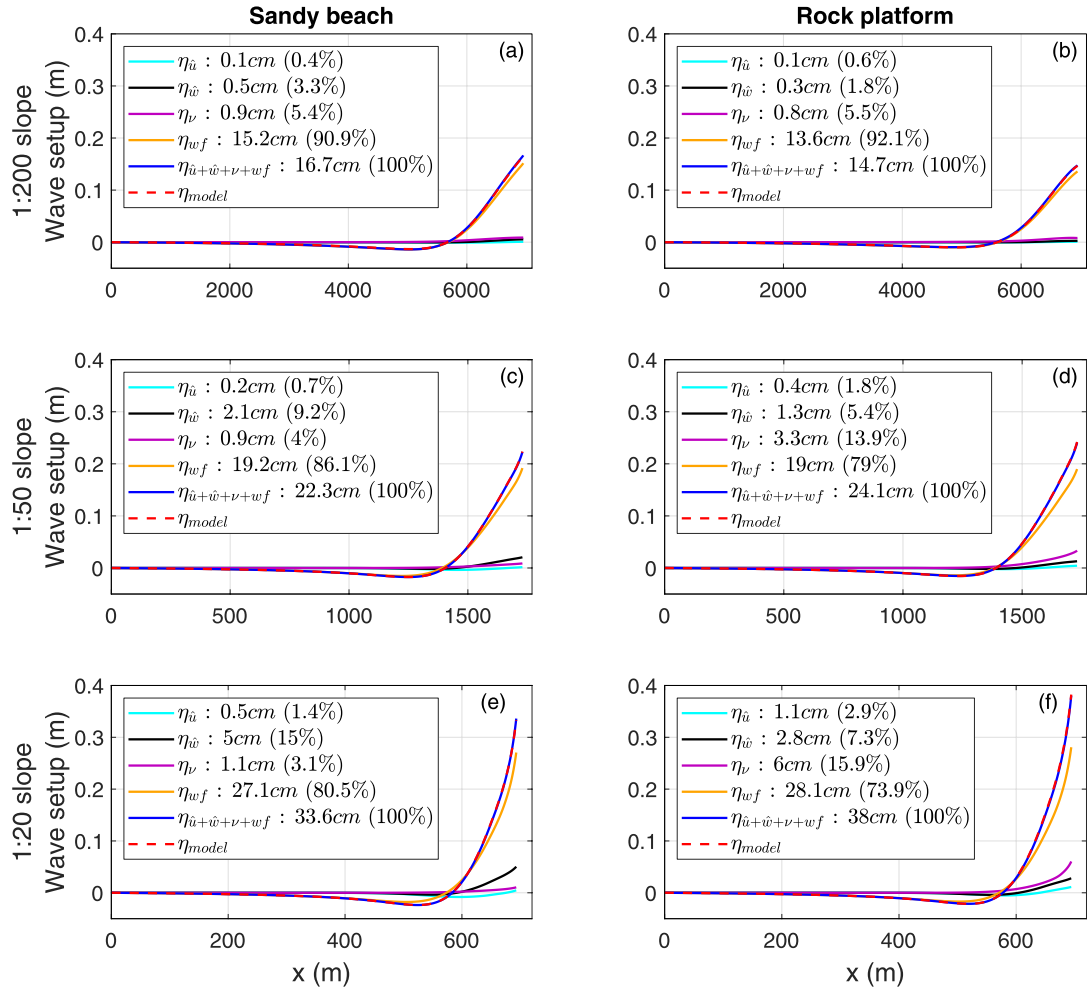

Figure 11. Contribution of each right-hand side terms of Equation 15 to the wave setup ($\eta_{\hat{u}}$, $\eta_{\hat{w}}$, η_{ν} and η_{wf}), total contribution of these terms ($\eta_{\hat{u}+\hat{w}+\nu+wf}$), compared to the wave setup obtained from the model (η_{model}), on a sandy beach and on a rock platform for 1:200, 1:50 and 1:20 slopes.

performed with three different constant slopes of 1:200, 1:50, and 1:20 and two different bottom types, a sandy beach and a rock platform (hereafter SB and RP respectively), such that the influence of both the gradient and nature of the bottom can be analyzed. The SB is characterized by a z_0 of 0.0001 m in the hydrodynamic model and a k_n of 0.05 m in the Madsen's formulation in the wave model while the RP is represented with the parameters of our real case ($z_0 = 0.02$ m and $k_n = 0.13$ m). Wave dissipation by depth-induced breaking is also calculated with van der Westhuysen (2010). The grid resolution ranges from 15 m at the open boundary to 2 m at the shoreline. A JONSWAP spectrum is prescribed at the ocean boundary, characterized by shore-normal incident waves of significant wave height of 3 m and peak period of 13 s. Tidal and atmospheric forcings are turned off. Under steady state, the wave setup is balanced by the following depth-integrated terms in the cross-shore momentum equation:

$$g\frac{\partial \eta}{\partial x} = \frac{1}{h}\int_{-d}^{\eta}\left(-\hat{u}\frac{\partial \hat{u}}{\partial x} - \hat{v}\frac{\partial \hat{u}}{\partial y} - \hat{w}\frac{\partial \hat{u}}{\partial z} + \frac{\partial}{\partial z}\left(\nu\frac{\partial \hat{u}}{\partial z}\right) + F_{wave,x}\right)dz \tag{15}$$

where $\hat{\mathbf{u}} = (\hat{u}, \hat{v}, \hat{w})$ is the quasi-Eulerian velocity and $F_{wave,x}$ is the cross-shore component of wave forces (see Appendix A1). Following the methodology of Guérin et al. (2018), the analysis is carried out by computing the contribution of each right-hand side (hereafter RHS) term of Equation 15 to the wave setup along a cross-shore profile from a water depth of 35 m to the shoreline (Figure 11). On this figure, $\eta_{\hat{u}}$, $\eta_{\hat{w}}$, η_{ν} correspond to the contribution of the terms associated with the wave-induced circulation, which are the horizontal (cross-shore)

advection, the vertical advection and the vertical viscosity terms respectively. η_{wf} is the contribution of the wave forces term. One should note that the contribution of the alongshore advection term ($\eta_{\hat{v}}$) is nil as waves are shore-normal. In Figure 11, the sum of the contribution of the RHS terms of Equation 15, $\eta_{\hat{u}+\hat{w}+v+wf}$, compares well with the wave setup obtained from the model, η_{model}, which shows that our momentum balance is accurately closed.

For all the simulations, wave forces are the main contributors to the wave setup, with η_{wf} representing between 74% and 92% of the total wave setup $\eta_{\hat{u}+\hat{w}+v+wf}$ (Figure 11). On both bottom types, the absolute value of the wave setup due to wave forces increases with the slope while their relative contribution decreases in favor to the terms associated with the wave-induced circulation. Among these terms, the vertical advection term becomes dominant for steeper SB, accounting for 15% of the wave setup for a 1:20 slope ($\eta_{\hat{w}}$, Figures 11a, 11c, and 11e). Note that Guérin et al. (2018) found a larger contribution of horizontal advection to wave setup, but these authors employed a simpler parameterization for vertical mixing, which results in more sheared currents and hence, a larger horizontal advection compared to the present study. For RP, the vertical viscosity term contributes the most to the wave setup (after wave forces), with larger importance as the slope steepens, reaching up to 16% on the 1:20 slope (η_{ν}, Figures 11b, 11d, and 11f). Regarding the differences between SB and RP, one can note that for a given slope, the contribution of the vertical advection term $\eta_{\hat{w}}$ is more important for SB than RP, which is explained by a higher (negative) vertical velocity in the surf zone of SB. In addition, the maximum of the undertow on RP is reached higher in the water column than on SB. As vertical gradients of the cross-shore velocity are negative from the bottom up to this point, the contribution of the depth-integrated vertical advection term to the wave setup is reduced for RP. Conversely, the vertical viscosity term appears to be more relevant on RP than on SB for a given slope. The increased bottom roughness z_0 modifies the vertical profile of the eddy viscosity and the vertical gradient of the cross-shore velocity in the lower part of the water column, which yields a greater contribution of the vertical viscosity term (η_{ν}).

Overall, the wave-induced circulation increasingly contributes to the wave setup with the slope, accounting for 20% for 1:20 sloping SB, which is in line with the results of Guérin et al. (2018), and up to 26% for 1:20 sloping RP. Therefore, this analysis reveals that a higher roughness enhances the contribution of the wave-induced circulation to the wave setup (mainly through the vertical viscosity term). Contrarily, wave dissipation by friction reduces the wave height before depth-induced breaking, resulting in a weaker wave setup due to wave forces for RP than SB of 1:200 slope, with η_{wf} = 15.2 and 13.6 cm respectively (Figures 11a and 11b). As the slope increases, less wave energy is dissipated by friction prior to wave breaking, yielding a comparable contribution of wave forces to wave setup for SB and RP.

In conclusion to this analysis, the roughness of the shore platform influences wave setup dynamics through two opposing mechanisms: (1) wave frictional effects prior to breaking reduce the wave setup and (2) the wave-induced circulation increases the wave setup, this process being enhanced by interactions with a rough bottom. These two counteracting effects of platform roughness on the wave setup corroborate the results of Buckley et al. (2016) on fringing reefs. Process (1) appears to be dominant on gently sloping rock platforms, as shown by the smaller wave setup for RP than SB of 1:200 slope (Comparison of $\eta_{\hat{u}+\hat{w}+v+wf}$ between Figures 11a and 11b). As the slope steepens, the effect of process (1) is reduced and that of process (2) increases, the latter becomes hence predominant over process (1), which leads to a larger wave setup for RP than SB (Comparison of $\eta_{\hat{u}+\hat{w}+v+wf}$ between Figures 11e and 11f). While we consider constant slopes in this analysis, the relative contribution of these mechanisms can be different depending of the platform geometry (various slopes, absence or presence of a seaward edge) and the roughness distribution on this variable geometry.

6. Conclusion

This study investigated the role of bed roughness on wave dissipation, mean circulation, and wave setup dynamics on a gently sloping shore platform. Two field experiments were conducted under fair weather and storm wave conditions. Data analysis was complemented with numerical simulations conducted with the fully coupled modeling system SCHISM with a vortex force formalism to represent the effects of short waves on the mean circulation. The results showed first that a bottom friction formulation that accounts for the bottom roughness of the platform is required to adequately model associated frictional effects. The correct representation of wave bottom friction, together with the adaptive depth-induced breaking formulation of Pezerat et al. (2021), led to quite

accurate wave and wave setup predictions at the coast. Further analysis conducted on the relative contribution of depth-induced breaking to wave bottom friction revealed that wave breaking is dominant in the surf zone, but frictional effects that occur from the subtidal zone account for 50% and 42% of the total wave energy dissipation in fair weather and storm wave conditions respectively. As an important effect, wave bottom friction decreases wave height before breaking, which in turn reduces the wave setup (mechanism 1). Conversely, an analysis of the cross-shore momentum balance on idealized rock platforms and sandy beaches revealed that the contribution of the wave-induced depth-varying circulation to the wave setup is enhanced over rough bottoms (mechanism 2), explaining up to 26% of the wave setup at the shoreline of 1:20 sloping shore platforms (mechanism 2). While mechanism 1 appears dominant over mechanism 2 on gently sloping shore platforms, a steeper slope would induce less wave frictional dissipation before breaking and a larger contribution of the depth-varying circulation to the wave setup, resulting in an increased wave setup compared to a sandy beach.

This study provides new insights into waves, currents and wave setup dynamics on shore platforms. Although wave transformation processes and the associated circulation were well predicted overall, further research is needed to better understand the contribution of the bottom streaming to the surf zone mean circulation and to verify the vertical distribution of the associated acceleration. This will imply new field experiments on shore platforms with high-resolution velocity measurements at several positions in the water column. In addition, the processes affecting wave setup dynamics on shore platforms highlighted in this study, in particular the contribution of the wave-induced circulation to the wave setup, will have to be verified on steeper shore platforms.

Improving knowledge of wave setup on shore platforms can help future research to quantify its contribution to erosion and debris removal at the cliff toe (Ogawa et al., 2015), but also to coastal flooding risks when platforms are backed by low-lying coasts (Didier et al., 2016; Naylor et al., 2014). Although sediment distribution in coastal zones is not always available, our study suggests that a physical representation of the bottom substrate in storm surge models, in particular nearshore rocky bottoms, improves waves, wave setup and thus storm surges predictions at the coast.

Appendix A: Modeling System

A1. Vortex Force Formalism

In the vortex force framework, the mass conservation and momentum equations of the hydrodynamic model read:

$$\nabla \cdot \hat{\mathbf{u}} = 0 \tag{A1}$$

$$\frac{D\hat{u}}{Dt} = f\hat{v} - \frac{1}{\rho}\frac{\partial P_A}{\partial x} - g\frac{\partial \eta}{\partial x} + \frac{\partial}{\partial z}\left(\nu\frac{\partial \hat{u}}{\partial z}\right) + F_{wave,x} \tag{A2}$$

$$\frac{D\hat{v}}{Dt} = -f\hat{u} - \frac{1}{\rho}\frac{\partial P_A}{\partial y} - g\frac{\partial \eta}{\partial y} + \frac{\partial}{\partial z}\left(\nu\frac{\partial \hat{v}}{\partial z}\right) + F_{wave,y} \tag{A3}$$

In Equation A1, $\nabla = \left(\frac{\partial}{\partial x}, \frac{\partial}{\partial y}, \frac{\partial}{\partial z}\right)$ and $\hat{\mathbf{u}} = (\hat{u}, \hat{v}, \hat{w})$ is the quasi-Eulerian velocity, equal to the mean Lagrangian velocity $\mathbf{u} = (u, v, w)$ minus the Stokes velocity $\mathbf{u_s} = (u_s, v_s, w_s)$. In Equations A2 and A3, f is the Coriolis parameter, ρ is the water density, P_A is the sea-level atmospheric pressure, g the acceleration due to gravity, η is the mean free surface elevation and ν is the vertical eddy viscosity. $F_{wave,x}$ and $F_{wave,y}$ are the two components of the wave forces (i.e., wave accelerations), given by:

$$F_{wave,x} = v_s\left[f + \left(\frac{\partial \hat{v}}{\partial x} - \frac{\partial \hat{u}}{\partial y}\right)\right] - w_s\frac{\partial \hat{u}}{\partial z} - \frac{\partial J}{\partial x} + \hat{F}_{br,x} + \hat{F}_{bot,x} \tag{A4}$$

$$F_{wave,y} = -u_s\left[f + \left(\frac{\partial \hat{v}}{\partial x} - \frac{\partial \hat{u}}{\partial y}\right)\right] - w_s\frac{\partial \hat{v}}{\partial z} - \frac{\partial J}{\partial y} + \hat{F}_{br,y} + \hat{F}_{bot,y} \tag{A5}$$

where J is the wave-induced mean pressure and $\hat{\boldsymbol{F}}_{br}$ and $\hat{\boldsymbol{F}}_{bot}$ terms are the non-conservative accelerations due to wave breaking modified by the action of surface rollers, and wave streaming respectively (see Section 3.3 for their expressions).

A2. Surface Roller Model

A new surface roller model has been implemented in WWM compared to the one used in Guérin et al. (2018). It is now based on the approach of Reniers et al. (2004) with minor adjustments. The evolution equation for the surface roller bulk energy E_{rol} can be read as follows (e.g., see Reniers et al., 2004):

$$\frac{\partial E_{rol}}{\partial t} + 2\nabla \cdot \left(c_p + \hat{\mathbf{U}}\right) E_{rol} = \alpha_r D_{br} - D_{rol} \tag{A6}$$

where c_p is the phase speed at the peak wave frequency and $\hat{\mathbf{U}} = \left(\hat{U}, \hat{V}\right)$ are the horizontal components of the depth-integrated quasi-Eulerian velocity. The roller dissipation rate D_{rol} can be computed as a function of wave and roller characteristics (i.e., Svendsen, 1984). However, there is some uncertainties regarding the empirical formulations of the roller area and the void ratio in rollers (Martins et al., 2018), it is thus preferred to calculate D_{rol} as a direct function of the roller energy E_{rol} following Reniers et al. (2004):

$$D_{rol} = \frac{2g\sin\beta E_{rol}}{c_p} \tag{A7}$$

where β is the angle at the wave/roller inner interface and $\sin\beta$ is set to the common value of 0.1 (Reniers et al., 2004).

Once accounting for surface rollers contribution, the horizontal Stokes Drift velocities read:

$$(u_s, v_s) = \int_0^{2\pi}\int_0^{\infty} (\cos\theta, \sin\theta)\, \sigma k(\sigma) E(\sigma,\theta) \frac{\cosh(2k(\sigma)(z+d))}{\sinh^2(k(\sigma)h)} d\sigma d\theta + 2\frac{E_{rol}}{\rho c_p h} (\cos\theta_m, \sin\theta_m) \tag{A8}$$

in which $h = d + \eta$ is the mean water depth and d is the bathymetry.

A3. Wave-Enhanced Turbulent Vertical Mixing

Wave breaking processes at the surface are an important source of turbulence which can greatly affect the vertical mixing in the water column (Agrawal et al., 1992). In SCHISM, the hydrodynamic model is coupled to the General Ocean Turbulence Model (GOTM; Umlauf et al., 2005) which solves a k-ω turbulence scheme, retrieved from the generic length scale two-equation turbulence closure model. The injection of TKE at the surface by breaking waves is modeled through the following flux-type boundary condition at the surface ($z = \eta$; Craig & Banner, 1994; Feddersen & Trowbridge, 2005):

$$\frac{\nu}{\sigma_q}\frac{\partial q}{\partial z} = F_q \left(\frac{z_0^s - z'}{z_0^s}\right)^{\frac{3}{2}\alpha} \tag{A9}$$

where ν is the vertical eddy viscosity, q is the TKE, σ_q is the turbulent Schmidt number for q, F_q [$m^3 \cdot s^{-3}$] is the flux of energy injected into the water column, α is the spatial decay rate in the wave-enhanced layer, z' is half the height of the top cell and z_0^s is the surface roughness length that dictates the distribution of the TKE in the water column. z_0^s has a strong influence on vertical profiles of currents but is difficult to measure, a number of parametrizations have thus been proposed for this quantity (Moghimi et al., 2016). It has been either defined as a constant ($z_0^s = 0.2$ m; Feddersen & Trowbridge, 2005) or proportional to the significant wave height H_{m0}: $z_0^s = \alpha_w H_{m0}$ (Terray et al., 1996) with α_w an O(1) parameter. The latter parameterization is used in the present study with α_w fixed to 0.8. Following the approach of Feddersen and Trowbridge (2005), F_q is assumed to be function of the energy dissipated by wave breaking and whitecapping at the surface:

$$F_q = \frac{c_{br}}{\rho}\left((1-\alpha_r) D_{br} + D_{rol}\right) - \frac{c_{ds}}{\rho}\int_0^{2\pi}\int_0^{\infty} \sigma S_{ds}(\sigma,\theta) d\sigma d\theta \tag{A10}$$

where c_{br} and c_{ds} control the amount of energy injected into the water column from wave breaking and whitecapping respectively. c_{br} can range between 0.01 and 0.25 according to Feddersen and Trowbridge (2005) while Bakhoday Paskyabi et al. (2012) suggested $c_{ds} \sim 1$. Here, the values of 0.15 for c_{br} and 1 for c_{ds} are retained.

At the bottom, a Dirichlet boundary condition is used:

$$q = \frac{u_*}{c_\mu^{0^2}}; \qquad u_* = \sqrt{\tau_{wc} + \sqrt{\hat{F}_{bot,x}^2 + \hat{F}_{bot,y}^2}} \tag{A11}$$

where c_μ^0 is a constant and u_* is the bottom friction velocity which is typically taken equal to $\sqrt{\tau_{wc}}$ where τ_{wc} is the wave-current bottoms stress (see Section 3.4). In this study, we account for the additional TKE produced by wave frictional dissipation, with $\hat{\boldsymbol{F}}_{bot}$ corresponding to the depth-integrated acceleration due to bottom friction.

Appendix B: Estimation of the Vertical Position of the Offshore Sensor

Figure B1a shows the mean free surface elevation η at the intertidal sensors at high tide on 12 March afternoon, which corresponds to the calmest conditions during the field campaign. The vertical position of PT 1 (in the subtidal zone) was determined at this instance, by assuming an horizontal plane between PT 1 and PT 4 (that is no contributions from surface stress or wave setup to the mean free surface elevation between PT 1 and PT 4). On Figure B1b, the mean free surface elevation was corrected from the modeled wave setup developed between the offshore PT (PT 1) and each sensor. At PT 4, the modeled wave setup is 0.01 m, which can support our assumption made in the determination of the vertical position of PT 1. Also, the resulting mean free surface elevation at all the intertidal sensors (from PT 4 to PT 10) are on a same horizontal plan (±0.01 m), which can attest of the accuracy of the leveling procedure.

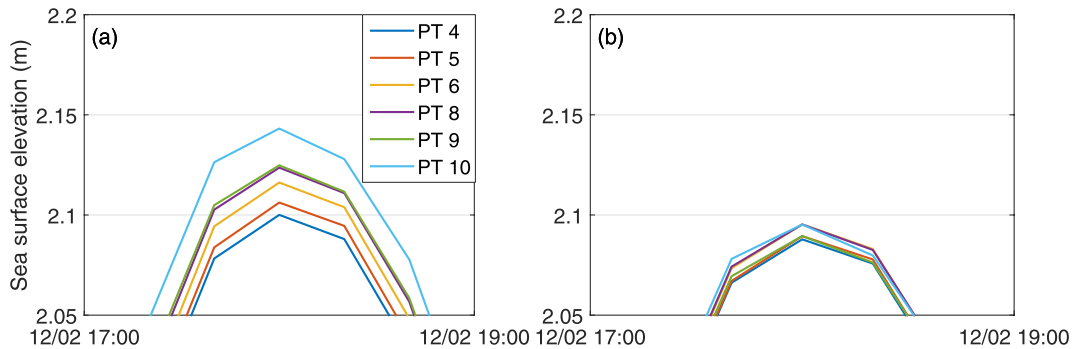

Figure B1. (a) Sea surface elevation on 12 March afternoon at high tide at the intertidal sensors without correction and (b) corrected from the wave setup obtained from the model.

Data Availability Statement

The processed field data and model input files used to run SCHISM-WWM simulations presented in this paper are available through a Zenodo repository (Lavaud et al., 2022). The instructions to download and install the model used in this study can be accessed freely at https://github.com/schism-dev/schism. Oléron wave buoy data were provided by CEREMA (http://candhis.cetmef.developpement-durable.gouv.fr) and atmospheric forcings originated from NCEP CFSR.

Acknowledgments
L. Lavaud is supported by a PhD fellowship from the Region Nouvelle-Aquitaine and the UNIMA engineering consulting company. K. Martins acknowledges the financial support from the University of Bordeaux, through an International Postdoctoral Grant (Idex, nb. 1024R-5030). M. Pezerat is supported by a PhD fellowship from CDA La Rochelle and from the FEDER project DURALIT. The field campaign conducted in February 2020 was partly funded by Observatoire de la Cote Aquitaine. Model developments on wave dissipation was a contribution of the project RISCO-BANGLA, funded by the interdisciplinary program "Défi Risques Naturels" of CNRS and IRD. The authors also greatly acknowledge SCHISM developers' community.

References

Acevedo-Ramirez, C. A., Stephenson, W., Wakes, S., & Mariño-Tapia, I. (2021). Wave transformation on a fringing reef system with spur and groove structures. *Journal of Geophysical Research: Oceans*, *126*(9), e2020JC016910. https://doi.org/10.1029/2020JC016910

Agrawal, Y., Terray, E., Donelan, M., Hwang, P., Williams, A., Drennan, W., et al. (1992). Enhanced dissipation of kinetic energy beneath surface waves. *Nature*, *359*(6392), 219–220. https://doi.org/10.1038/359219a0

Apotsos, A., Raubenheimer, B., Elgar, S., Guza, R. T., & Smith, J. A. (2007). Effects of wave rollers and bottom stress on wave setup. *Journal of Geophysical Research*, *112*(C2), C02003. https://doi.org/10.1029/2006JC003549

Ardhuin, F., Rascle, N., & Belibassakis, K. (2008). Explicit wave-averaged primitive equations using a generalized Lagrangian mean. *Ocean Modelling*, *20*(1), 35–60. https://doi.org/10.1016/j.ocemod.2007.07.001

Bakhoday Paskyabi, M., Fer, I., & Jenkins, A. D. (2012). Surface gravity wave effects on the upper ocean boundary layer: Modification of a one-dimensional vertical mixing model. *Continental Shelf Research*, *38*, 63–78. https://doi.org/10.1016/j.csr.2012.03.002

Battjes, J. A., & Stive, M. J. F. (1985). Calibration and verification of a dissipation model for random breaking waves. *Journal of Geophysical Research*, *90*(C5), 9159–9167. https://doi.org/10.1029/JC090iC05p09159

Beetham, E. P., & Kench, P. S. (2011). Field observations of infragravity waves and their behaviour on rock shore platforms. *Earth Surface Processes and Landforms*, *36*(14), 1872–1888. https://doi.org/10.1002/esp.2208

Bennis, A.-C., Ardhuin, F., & Dumas, F. (2011). On the coupling of wave and three-dimensional circulation models: Choice of theoretical framework, practical implementation and adiabatic tests. *Ocean Modelling*, *40*(3), 260–272. https://doi.org/10.1016/j.ocemod.2011.09.003

Bertin, X., Bruneau, N., Breilh, J.-F., Fortunato, A. B., & Karpytchev, M. (2012). Importance of wave age and resonance in storm surges: The case Xynthia, Bay of Biscay. *Ocean Modelling*, *42*, 16–30. https://doi.org/10.1016/j.ocemod.2011.11.001

Bertin, X., Li, K., Roland, A., & Bidlot, J.-R. (2015). The contribution of short-waves in storm surges: Two case studies in the Bay of Biscay. *Continental Shelf Research*, *96*, 1–15. https://doi.org/10.1016/j.csr.2015.01.005

Bertin, X., Martins, K., de Bakker, A., Chataigner, T., Guérin, T., Coulombier, T., & de Viron, O. (2020). Energy transfers and reflection of infragravity waves at a dissipative beach under storm waves. *Journal of Geophysical Research: Oceans*, *125*(5), e2019JC015714. https://doi.org/10.1029/2019JC015714

Bidlot, J.-R., Holmes, D. J., Wittmann, P. A., Lalbeharry, R., & Chen, H. S. (2002). Intercomparison of the performance of operational ocean wave forecasting systems with buoy data. *Weather and Forecasting*, *17*(2), 287–310. https://doi.org/10.1175/1520-0434(2002)017<0287:IOTPOO>2.0.CO;2

Bishop, C. T., & Donelan, M. A. (1987). Measuring waves with pressure transducers. *Coastal Engineering*, *11*(4), 309–328. https://doi.org/10.1016/0378-3839(87)90031-7

Blain, C. A., Westerink, J. J., & Luettich, R. A., Jr. (1994). The influence of domain size on the response characteristics of a hurricane storm surge model. *Journal of Geophysical Research*, *99*(C9), 18467–18479. https://doi.org/10.1029/94JC01348

Bowen, A. J., Inman, D. L., & Simmons, V. P. (1968). Wave 'set-down' and set-up. *Journal of Geophysical Research*, *73*(8), 2569–2577. https://doi.org/10.1029/JB073i008p02569

Bretschneider, C., Krock, H., Nakazaki, E., & Casciano, F. (1986). *Roughness of typical Hawaiian terrain for tsunami run-up calculations: A users manual* (p. 42). JKK Look Laboratory Report, University of Hawaii.

Buckley, M. L., Lowe, R. J., Hansen, J. E., & Van Dongeren, A. R. (2016). Wave setup over a fringing reef with large bottom roughness. *Journal of Physical Oceanography*, *46*(8), 2317–2333. https://doi.org/10.1175/JPO-D-15-0148.1

Castelle, B., Scott, T., Brander, R., & McCarroll, R. (2016). Rip current types, circulation and hazard. *Earth-Science Reviews*, *163*, 1–21. https://doi.org/10.1016/j.earscirev.2016.09.008

Craig, P. D., & Banner, M. L. (1994). Modeling wave-enhanced turbulence in the ocean surface layer. *Journal of Physical Oceanography*, *24*(12), 2546–2559. https://doi.org/10.1175/1520-0485(1994)024<2546:MWETIT>2.0.CO;2

Dean, R. G., & Bender, C. J. (2006). Static wave setup with emphasis on damping effects by vegetation and bottom friction. *Coastal Engineering*, *53*(2), 149–156. https://doi.org/10.1016/j.coastaleng.2005.10.005

Deigaard, R. (1993). A note on the three-dimensional shear stress distribution in a surf zone. *Coastal Engineering*, *20*(1), 157–171. https://doi.org/10.1016/0378-3839(93)90059-H

Delpey, M. T., Ardhuin, F., Otheguy, P., & Jouon, A. (2014). Effects of waves on coastal water dispersion in a small estuarine bay. *Journal of Geophysical Research: Oceans*, *119*(1), 70–86. https://doi.org/10.1002/2013JC009466

Didier, D., Bernatchez, P., Marie, G., & Boucher-Brossard, G. (2016). Wave runup estimations on platform-beaches for coastal flood hazard assessment. *Natural Hazards*, *83*(3), 1443–1467. https://doi.org/10.1007/s11069-016-2399-5

Dodet, G., Bertin, X., Bouchette, F., Gravelle, M., Testut, L., & Wöppelmann, G. (2019). Characterization of sea-level variations along the metropolitan coasts of France: Waves, tides, storm surges and long-term changes. *Journal of Coastal Research*, *88*(sp1), 10–24. https://doi.org/10.2112/SI88-003.1

Donelan, M. A., Dobson, F. W., Smith, S. D., & Anderson, R. J. (1993). On the dependence of sea surface roughness on wave development. *Journal of Physical Oceanography*, *23*(9), 2143–2149. https://doi.org/10.1175/1520-0485(1993)023<2143:OTDOSS>2.0.CO;2

Eldeberky, Y. (1996). *Nonlinear transformation of wave spectra in the nearshore zone* (Ph. D. thesis). Delft University of Technology, Department of Civil Engineering.

Eldeberky, Y., & Battjes, J. A. (1996). Spectral modeling of wave breaking: Application to Boussinesq equations. *Journal of Geophysical Research: Oceans*, *101*(C1), 1253–1264. https://doi.org/10.1029/95JC03219

Farrell, E., Granja, H., Cappietti, L., Ellis, J., Li, B., & Sherman, D. (2009). Wave transformation across a rock platform, Belinho, Portugal. *Journal of Coastal Research*, 44–48.

Feddersen, F., & Trowbridge, J. H. (2005). The effect of wave breaking on surf-zone turbulence and alongshore currents: A modeling study. *Journal of Physical Oceanography*, *35*(11), 2187–2203. https://doi.org/10.1175/JPO2800.1

Fredsøe, J., & Deigaard, R. (1992). *Mechanics of coastal sediment transport*. World Scientific. https://doi.org/10.1142/1546

Gon, C. J., MacMahan, J. H., Thornton, E. B., & Denny, M. (2020). Wave dissipation by bottom friction on the inner shelf of a rocky shore. *Journal of Geophysical Research: Oceans*, *125*(10), e2019JC015963. https://doi.org/10.1029/2019JC015963

Guérin, T., Bertin, X., Coulombier, T., & de Bakker, A. (2018). Impacts of wave-induced circulation in the surf zone on wave setup. *Ocean Modelling*, *123*, 86–97. https://doi.org/10.1016/j.ocemod.2018.01.006

Guza, R. T., & Thornton, E. B. (1981). Wave set-up on a natural beach. *Journal of Geophysical Research*, *86*(C5), 4133–4137. https://doi.org/10.1029/JC086iC05p04133

Hasselmann, K., Barnett, T., Bouws, E., Carlson, H., Cartwright, D., Enke, K., et al. (1973). Measurements of wind-wave growth and swell decay during the Joint North Sea Wave Project (JONSWAP). *Deutsche Hydrographische Zeitschrift*, *8*, 1–95.

Hasselmann, S., Hasselmann, K., Allender, J., & Barnett, T. (1985). Computations and parameterizations of the nonlinear energy transfer in a gravity-wave spectrum. Part II: Parameterizations of the nonlinear energy transfer for application in wave models. *Journal of Physical Oceanography*, *15*(11), 1378–1391. https://doi.org/10.1175/1520-0485(1985)015<1378:CAPOTN>2.0.CO;2

Janssen, P. A. (1991). Quasi-linear theory of wind-wave generation applied to wave forecasting. *Journal of Physical Oceanography*, *21*(11), 1631–1642. https://doi.org/10.1175/1520-0485(1991)021<1631:QLTOWW>2.0.CO;2

Jonsson, I. G. (1967). Wave boundary layers and friction factors. In *Coastal engineering* (Vol. 1966, pp. 127–148). https://doi.org/10.1061/9780872620087.010

Kennedy, D. M. (2015). Where is the seaward edge? A review and definition of shore platform morphology. *Earth-Science Reviews*, *147*, 99–108. https://doi.org/10.1016/j.earscirev.2015.05.007

Klopman, G. (1994). Stokes transport. *WL-Delft Hydraulics Report H840.30, Part II*.

Komen, G. J., Cavaleri, L., Donelan, M., Hasselmann, K., Hasselmann, S., & Janssen, P. A. E. M. (1994). *Dynamics and modelling of ocean waves*. Cambridge University Press. https://doi.org/10.1017/CBO9780511628955

Kowalczyk, H. (2016). *Wave transformation at a rock platform in Victoria, Australia - A study combining field measurements with numerical modelling*. (Student Paper).

Kranenburg, W. M., Ribberink, J. S., Uittenbogaard, R. E., & Hulscher, S. J. M. H. (2012). Net currents in the wave bottom boundary layer: On waveshape streaming and progressive wave streaming. *Journal of Geophysical Research: Earth Surface*, *117*(F3). https://doi.org/10.1029/2011JF002070

Lavaud, L., Bertin, X., Martins, K., Pezerat, M., Coulombier, T., & Dausse, D. (2022). Wave dissipation and mean circulation on a shore platform under storm wave conditions [Dataset]. Zenodo. https://doi.org/10.5281/zenodo.6048011
Lavaud, L., Bertin, X., Martins, K., Arnaud, G., & Bouin, M.-N. (2020). The contribution of short-wave breaking to storm surges : The case Klaus in the Southern Bay of Biscay. *Ocean Modelling*, *156*, 101710. https://doi.org/10.1016/j.ocemod.2020.101710
Lavaud, L., Pezerat, M., Coulombier, T., Bertin, X., & Martins, K. (2020). Hydrodynamics on a rocky shore under moderate-energy wave conditions. *Journal of Coastal Research*, *95*(SI), 1473–1479. https://doi.org/10.2112/SI95-284.1
Lentz, S., & Raubenheimer, B. (1999). Field observations of wave setup. *Journal of Geophysical Research*, *104*(C11), 25867–25875. https://doi.org/10.1029/1999JC900239
Longuet-Higgins, M. S. (1953). Mass transport in water waves. *Philosophical Transactions of the Royal Society of London. Series A, Mathematical and Physical Sciences*, *A245*(903), 535–581. https://doi.org/10.1098/rsta.1953.0006
Longuet-Higgins, M. S. (1970a). Longshore currents generated by obliquely incident sea waves: 1. *Journal of Geophysical Research*, *75*(33), 6778–6789. https://doi.org/10.1029/JC075i033p06778
Longuet-Higgins, M. S. (1970b). Longshore currents generated by obliquely incident sea waves: 2. *Journal of Geophysical Research*, *75*(33), 6790–6801. https://doi.org/10.1029/JC075i033p06790
Longuet-Higgins, M. S., & Stewart, R. (1962). Radiation stress and mass transport in gravity waves, with application to 'surf beats'. *Journal of Fluid Mechanics*, *13*(4), 481–504. https://doi.org/10.1017/S0022112062000877
Longuet-Higgins, M. S., & Stewart, R. (1964). Radiation stresses in water waves; A physical discussion, with applications. *Deep-Sea Research and Oceanographic Abstracts*, *11*(4), 529–562. https://doi.org/10.1016/0011-7471(64)90001-4
Lowe, R. J., Falter, J. L., Bandet, M. D., Pawlak, G., Atkinson, M. J., Monismith, S. G., & Koseff, J. R. (2005). Spectral wave dissipation over a barrier reef. *Journal of Geophysical Research*, *110*(C4), C04001. https://doi.org/10.1029/2004JC002711
Lowe, R. J., Falter, J. L., Monismith, S. G., & Atkinson, M. J. (2009). Wave-driven circulation of a coastal reef-lagoon system. *Journal of Physical Oceanography*, *39*(4), 873–893. https://doi.org/10.1175/2008JPO3958.1
Madsen, O. S., Poon, Y.-K., & Graber, H. C. (1989). Spectral wave attenuation by bottom friction: Theory. In *Coastal engineering* (Vol. 1988, pp. 492–504). https://doi.org/10.1061/9780872626874.035
Marshall, R. J., & Stephenson, W. J. (2011). The morphodynamics of shore platforms in a micro-tidal setting: Interactions between waves and morphology. *Marine Geology*, *288*(1), 18–31. https://doi.org/10.1016/j.margeo.2011.06.007
Martins, K., Blenkinsopp, C. E., Deigaard, R., & Power, H. E. (2018). Energy dissipation in the inner surf zone: New insights from LiDAR-based roller geometry measurements. *Journal of Geophysical Research: Oceans*, *123*(5), 3386–3407. https://doi.org/10.1029/2017JC013369
Mastenbroek, C., Burgers, G., & Janssen, P. (1993). The dynamical coupling of a wave model and a storm surge model through the atmospheric boundary layer. *Journal of Physical Oceanography*, *23*(8), 1856–1866. https://doi.org/10.1175/1520-0485(1993)023<1856:TDCOAW>2.0.CO;2
McCall, R. T., Masselink, G., Austin, M., Poate, T., & Jager, T. (2017). Modelling incident-band and infra gravity wave dynamics on rocky shore platforms. In *Coastal dynamics* (Vol. 2017).
Moghimi, S., Thomson, J., Özkan Haller, T., Umlauf, L., & Zippel, S. (2016). On the modeling of wave-enhanced turbulence nearshore. *Ocean Modelling*, *103*, 118–132. (Waves and coastal, regional and global processes). https://doi.org/10.1016/j.ocemod.2015.11.004
Naylor, L. A., Kennedy, D. M., & Stephenson, W. J. (2014). Chapter 17 Synthesis and conclusion to the rock coast geomorphology of the world. *Geological Society, London, Memoirs*, *40*(1), 283–286. https://doi.org/10.1144/M40.17
Naylor, L. A., & Stephenson, W. J. (2010). On the role of discontinuities in mediating shore platform erosion. *Geomorphology*, *114*(1), 89–100. (Rock Coast Geomorphology). https://doi.org/10.1016/j.geomorph.2008.12.024
Naylor, L. A., Stephenson, W. J., & Trenhaile, A. S. (2010). Rock coast geomorphology: Recent advances and future research directions. *Geomorphology*, *114*(1), 3–11. (Rock Coast Geomorphology). https://doi.org/10.1016/j.geomorph.2009.02.004
Ogawa, H. (2013). Observation of wave transformation on a sloping type B shore platform under wind-wave and swell conditions. *Geo-Marine Letters*, *33*(1), 1–11. https://doi.org/10.1007/s00367-012-0303-1
Ogawa, H., Dickson, M., & Kench, P. (2011). Wave transformation on a sub-horizontal shore platform, Tatapouri, North Island, New Zealand. *Continental Shelf Research*, *31*(14), 1409–1419. https://doi.org/10.1016/j.csr.2011.05.006
Ogawa, H., Dickson, M. E., & Kench, P. S. (2015). Hydrodynamic constraints and storm wave characteristics on a sub-horizontal shore platform. *Earth Surface Processes and Landforms*, *40*(1), 65–77. https://doi.org/10.1002/esp.3619
Ogawa, H., Kench, P., & Dickson, M. (2012). Field measurements of wave characteristics on a near-horizontal shore platform, Mahia Peninsula, North Island, New Zealand. *Geographical Research*, *50*(2), 179–192. https://doi.org/10.1111/j.1745-5871.2011.00715.x
Oh, J.-E., Jeong, W.-M., Chang, Y. S., & Oh, S.-H. (2020). On the separation period discriminating gravity and infragravity waves off Gyeongpo Beach, Korea. *Journal of Marine Science and Engineering*, *8*(3), 167. https://doi.org/10.3390/jmse8030167
Oliveira, A., Fortunato, A., Rogeiro, J., Teixeira, J., Azevedo, A., Lavaud, L., et al. (2020). OPENCoastS: An open-access service for the automatic generation of coastal forecast systems. *Environmental Modelling & Software*, *124*, 104585. https://doi.org/10.1016/j.envsoft.2019.104585
Pezerat, M., Bertin, X., Martins, K., Mengual, B., & Hamm, L. (2021). Simulating storm waves in the nearshore area using spectral model: Current issues and a pragmatic solution. *Ocean Modelling*, *158*, 101737. https://doi.org/10.1016/j.ocemod.2020.101737
Poate, T., Masselink, G., Austin, M. J., Dickson, M., & McCall, R. (2018). The role of bed roughness in wave transformation across sloping rock shore platforms. *Journal of Geophysical Research: Earth Surface*, *123*(1), 97–123. https://doi.org/10.1002/2017JF004277
Pond, S., & Pickard, G. (1983). *Introductory dynamical oceanography*. Butterworth Heinemann.
Raubenheimer, B., Guza, R., & Elgar, S. (2001). Field observations of wave-driven setdown and setup. *Journal of Geophysical Research*, *106*(C3), 4629–4638. https://doi.org/10.1029/2000JC000572
Reniers, A., Thornton, E., Stanton, T., & Roelvink, J. (2004). Vertical flow structure during Sandy Duck: Observations and modeling. *Coastal Engineering*, *51*(3), 237–260. https://doi.org/10.1016/j.coastaleng.2004.02.001
Roelvink, J. A., & Stive, M. J. F. (1989). Bar-generating cross-shore flow mechanisms on a beach. *Journal of Geophysical Research*, *94*(C4), 4785–4800. https://doi.org/10.1029/JC094iC04p04785
Roland, A., & Ardhuin, F. (2014). On the developments of spectral wave models: Numerics and parameterizations for the coastal ocean. *Ocean Dynamics*, *64*(6), 833–846. https://doi.org/10.1007/s10236-014-0711-z
Roland, A., Zhang, Y. J., Wang, H. V., Meng, Y., Teng, Y.-C., Maderich, V., et al. (2012). A fully coupled 3D wave-current interaction model on unstructured grids. *Journal of Geophysical Research: Oceans*, *117*(C11). https://doi.org/10.1029/2012JC007952
Saha, S., Moorthi, S., Pan, H.-L., Wu, X., Wang, J., Nadiga, S., et al. (2010). The NCEP climate forecast system reanalysis. *Bulletin of the American Meteorological Society*, *91*(8), 1015–1058. https://doi.org/10.1175/2010BAMS3001.1
Savige, T. R., Kowalczyk, H. E., Fellowes, T. E., & Kennedy, D. M. (2021). The role of seaward morphology on wave transformation onto and across a microtidal shore platform. *Continental Shelf Research*, *224*, 104472. https://doi.org/10.1016/j.csr.2021.104472
Soulsby, R. (1997). *Dynamics of marine sands*. Thomas Telford Publishing. https://doi.org/10.1680/doms.25844

Stephenson, W. J. (2000). Shore platforms: A neglected coastal feature? *Progress in Physical Geography: Earth and Environment*, *24*(3), 311–327. https://doi.org/10.1177/030913330002400301

Stephenson, W. J., & Kirk, R. M. (2000). Development of shore platforms on Kaikoura Peninsula, South Island, New Zealand: Part One: The role of waves. *Geomorphology*, *32*(1), 21–41. https://doi.org/10.1016/S0169-555X(99)00061-6

Stephenson, W. J., Naylor, L. A., Smith, H., Chen, B., & Brayne, R. P. (2018). Wave transformation across a macrotidal shore platform under low to moderate energy conditions. *Earth Surface Processes and Landforms*, *43*(1), 298–311. https://doi.org/10.1002/esp.4245

Stephenson, W. J., & Thornton, L. E. (2005). Australian rock coasts: Review and prospects. *Australian Geographer*, *36*(1), 95–115. https://doi.org/10.1080/00049180500050946

Stive, M., & Wind, H. (1982). A study of radiation stress and set-up in the nearshore region. *Coastal Engineering*, *6*(1), 1–25. https://doi.org/10.1016/0378-3839(82)90012-6

Sunamura, T. (1992). Geomorphology of rocky coasts. John Wiley & Sons, Chichester.

Svendsen, I. (1984). Wave heights and set-up in a surf zone. *Coastal Engineering*, *8*(4), 303–329. https://doi.org/10.1016/0378-3839(84)90028-0

Terray, E., Donelan, M., Agrawal, Y., Drennan, W., Kahma, K., Williams, A., et al. (1996). Estimates of kinetic energy dissipation under breaking waves. *Journal of Physical Oceanography*, *26*(5), 792–807. https://doi.org/10.1175/1520-0485(1996)026<0792:EOKEDU>2.0.CO;2

Thornton, E. B., & Guza, R. T. (1986). Surf zone longshore currents and random waves: Field data and models. *Journal of Physical Oceanography*, *16*(7), 1165–1178. https://doi.org/10.1175/1520-0485(1986)016<1165:SZLCAR>2.0.CO;2

Trenhaile, A. (1987). *The geomorphology of rock coasts*. Clarendon Press, Oxford.

Trenhaile, A. S., & Kanyaya, J. I. (2007). The role of wave erosion on sloping and horizontal shore platforms in macro-and mesotidal environments. *Journal of Coastal Research*, *23*(2), 298–309. https://doi.org/10.2112/04-0282.1

Trowbridge, J., & Madsen, O. S. (1984). Turbulent wave boundary layers: 2. Second-order theory and mass transport. *Journal of Geophysical Research*, *89*(C5), 7999–8007. https://doi.org/10.1029/JC089iC05p07999

Uchiyama, Y., McWilliams, J. C., & Shchepetkin, A. F. (2010). Wave–current interaction in an oceanic circulation model with a vortex-force formalism: Application to the surf zone. *Ocean Modelling*, *34*(1), 16–35. https://doi.org/10.1016/j.ocemod.2010.04.002

Umlauf, L., Burchard, H., & Bolding, K. (2005). *GOTM-scientific documentation: Version 3.2*. Institut für Ostseeforschung.

van der Westhuysen, A. J. (2010). Modeling of depth-induced wave breaking under finite depth wave growth conditions. *Journal of Geophysical Research: Oceans*, *115*(C1), C01008. https://doi.org/10.1029/2009JC005433

Wang, P., McWilliams, J. C., Uchiyama, Y., Chekroun, M. D., & Yi, D. L. (2020). Effects of wave streaming and wave variations on nearshore wave-driven circulation. *Journal of Physical Oceanography*, *50*(10), 3025–3041. https://doi.org/10.1175/JPO-D-19-0304.1

Xie, M., Zhang, C., Li, J., Li, S., Yang, Z., Zhang, H., & Qu, K. (2021). Flow structure and bottom friction of the nonlinear turbulent boundary layer under stormy waves. *Coastal Engineering*, *164*, 103811. https://doi.org/10.1016/j.coastaleng.2020.103811

Zhang, Y., & Baptista, A. M. (2008). SELFE: A semi-implicit Eulerian–Lagrangian finite-element model for cross-scale ocean circulation. *Ocean Modelling*, *21*(3), 71–96. https://doi.org/10.1016/j.ocemod.2007.11.005

Zhang, Y. J., Ateljevich, E., Yu, H.-C., Wu, C. H., & Yu, J. C. (2015). A new vertical coordinate system for a 3D unstructured-grid model. *Ocean Modelling*, *85*, 16–31. https://doi.org/10.1016/j.ocemod.2014.10.003

Zhang, Y. J., Ye, F., Stanev, E. V., & Grashorn, S. (2016). Seamless cross-scale modeling with SCHISM. *Ocean Modelling*, *102*, 64–81. https://doi.org/10.1016/j.ocemod.2016.05.002

Zheng, L., Weisberg, R. H., Huang, Y., Luettich, R. A., Westerink, J. J., Kerr, P. C., et al. (2013). Implications from the comparisons between two- and three-dimensional model simulations of the Hurricane Ike storm surge. *Journal of Geophysical Research: Oceans*, *118*(7), 3350–3369. https://doi.org/10.1002/jgrc.20248